POLYMER DROPLETS LEVELLING ON THIN FILMS OF IDENTICAL POLYMER

POLYMER DROPLETS LEVELLING ON THIN FILMS OF IDENTICAL POLYMER

By

SARA LOUISE CORMIER, B.Sc.

A Thesis
Submitted to the School of Graduate Studies
in Partial Fulfillment of the Requirements
for the Degree
Master of Science

McMaster University

MASTER OF SCIENCE (2012)
(Physics)

McMaster University
Hamilton, Ontario

TITLE: Polymer Droplets Levelling on Thin Films of Identical Polymer

AUTHOR: Sara Louise Cormier, B.Sc.(McMaster University)

SUPERVISOR: Dr. Kari Dalnoki-Veress

NUMBER OF PAGES: viii, 62

Abstract

This thesis describes the experimental results of liquid polymer droplets levelling on thin films of identical polymer liquid. Through varying the thickness of the underlying polymer film relative to the size of the droplet height, we have observed a crossover in the dynamics between droplets spreading on very thin films to droplets levelling on films thicker than the droplet itself. In the thin film regime, the underlying film behaves as a pre-existing precursor film and the droplet spreads according to the well-known Tanner's law where the droplet height, d_0, decreases in time as $d_0 \sim t^{-1/5}$. In the opposite regime, when the film thickness is much greater than the initial droplet height, the droplet levels with a much stronger time dependence compared to Tanner's law spreading, $d_0 \sim t^{-1/2}$. Not only have we observed the two extreme cases, we have also experimentally observed levelling behaviour of intermediate systems, where the droplet height and film height are on the same order. We have captured experimentally the crossover behaviour of droplets spreading on thin films to droplets levelling on thick films. In addition, we have developed a theoretical model that accurately captures the physics of this crossover using the lubrication approximation for thin film flows. The relevant background information will be presented as well as a detailed description of the sample preparation techniques required to fabricate spherical caps atop thin films of identical material.

Acknowledgements

I have procrastinated writing the acknowledgement part of my thesis for far too long. I think, in part, I am nervous that I will not be able to accurately thank all the wonderful people that have helped me complete this degree. The other part is that I do not like writing. I have, however, realized that no matter how long I wait to write this I will never be able to properly put into words how I feel, and how thankful I am to the phenomenal people in my life. I will nevertheless do my best.

First and foremost I would like to thank my supervisor Kari. His passion for science is infectious and always helps to motivate me. He has given me confidence when I needed it and always knows how to gently encourage and push me a little more than I thought possible. He is my role model. My pseudo-supervisor and lab-mate Josh. Thank you so much for your continued patience in teaching me (especially MATLAB) and with helping me through the paper writing process. To all our our lab group, past and present, for all the fruitful discussions. I love the excitement for science that everyone shares and the unique negative reinforcement that only our lab has. I think you are supposed to dread group meetings but with our group I have always looked forward to them.

Outside the department, I am indebted to my family, parents Tom and Cathy and sister Molly, for supporting me emotionally since the very beginning. They have always believed in me and kept me grounded, and their support has made all the difference. I would also like to thank all my wonderful friends who have always helped me to de-stress when I needed it most. Lastly, I cannot ever express the extent of my gratitude to my best friend and fiancé Michael. From sitting through countless practice talks to helping plan more than his fair share of our wedding while I completed this degree, he has been there to support me every step of this journey. I truly would not have been able to do this without his love and encouragement. I feel so very lucky to have such an incredible partner.

Contents

List of Figures

Chapter 1

Introduction

Understanding the behaviour of fluids and their wetting properties is relevant to a wide variety of applications such as preparation of liquid coatings for use in spraying paint, electronic coatings, and coatings on items such as automobiles and windshields. In addition, applications such as ink jet printing require knowledge of wetting and spreading to produce high quality, reproducible images. This thesis seeks to expand on the already large body of knowledge related to the field of wetting and spreading of thin liquid films. Specifically, we have investigated the behaviour of small micron-sized polymer droplets levelling on thin films of identical polymer. By varying the thickness of the substrate film relative to the initial droplet height we have observed a crossover in the power law dependence between droplets spreading on very thin films (Tanner's law) to droplets levelling on very thick films.

First, in Chapter 2, a brief review of the relevant concepts related to this project will be presented. An understanding of why some liquids wet substrates while others do not will be discussed along with the phenomenon of dewetting. A description of the lubrication approximation as it relates to thin film flows will be provided. Tanner's law which explains the spreading behaviour of small droplets on completely wetting substrates will be derived and a brief overview of the literature related to spreading of droplets will be presented. Polymers are a unique class of materials that are ideal for studing the flow behaviour of thin films. The properties that make polymers ideal to work with experimentally will also be discussed. Lastly, a basic understanding of ellipsometry and atomic force microscopy will be developed as these experimental tools are utilized in this experiment.

The research field of droplet spreading has been heavily studied both experimentally, theoretically and computationally as will be discussed in Chapter 2. However, to our knowledge, liquid droplets spreading on identical liquid films have not been observed previously, perhaps due to difficulties in preparing well controlled samples. In Chapter 3, a detailed description of our sample preparation technique which includes spincasting, dewetting and floating will be provided. This technique allows for well-controlled sample preparation resulting in the desired geometry of a perfectly spherical cap atop a thin film of identical material. The method of analysis using MATLAB will also be presented.

In Chapter 4, a scaling model based on the lubrication approximation for thin film flows that was developed in conjunction with our collaborators at the ESPCI in Paris, France will be derived. This model effectively captures the crossover behaviour of our system. A full description of the model along with our experimental results is summarized in a paper that has been submitted to Physical Review Letters and has been inserted into Chapter 5.

Ultimately, we will present the levelling behaviour of polymer droplets on thin liquid films of identical polymer. We will show that this levelling behaviour is dependent on the aspect ratio between droplet height to film height and that the physics of this behvaiour is well described by our theoretical model.

Chapter 2

Review

2.1 Wetting, Spreading and Dewetting

The purpose of the research is to investigate the spreading behaviour of micron-sized liquid droplets. Spreading and wetting of liquids is an intense research area and many in-depth reviews on the subject exist in literature [1–9]. To understand this subject we must first develop an understanding as to why some liquids spread while others do not. Take for example a drop of water; if the drop of water is on a waxy surface, the droplet does not spread and maintains a high contact angle. The contact angle is defined as the angle between the surface and the liquid as shown schematically in Fig 2.1. On the other hand, if a droplet of water falls on an uncoated, clean glass surface, the water drop will spread completely leaving a thin water film on the glass surface. The spreading parameter, S, determines if a liquid will wet a surface or not. The spreading parameter is the difference in surface energy per unit area of a dry versus a wet surface,

$$S = [E_{substrate}]_{dry} - [E_{substrate}]_{wet}, \tag{2.1}$$

where $[E_{substrate}]_{dry}$ is the surface energy of the dry substrate and $[E_{substrate}]_{wet}$ is the surface energy of the wet substrate. If $S > 0$, the liquid will wet the surface completely as this will be the lowest energy state. In this case, the equilibrium configuration is that of a flat liquid film. On the other hand, if $S < 0$, the liquid will not wet the surface completely and will instead form a spherical cap (or flattened spherical cap if gravity effects are important [10]) with some equilibrium contact angle, θ_E [6]. The

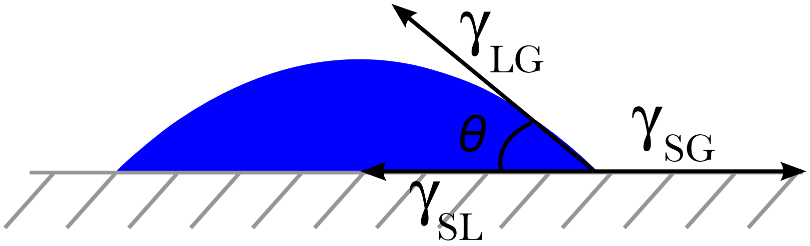

Figure 2.1:
Schematic of a liquid drop on a solid surface with contact angle θ. The surface tension, γ, between the three different interfaces, solid/liquid, solid/gas and liquid/gas are also shown as described in the Young-Dupré equation, Eq. 2.4.

spreading parameter is dependent on the temperature. If the temperature of a system is varied, a wetting transitions can be observed for which the liquid transitions from the case of incomplete wetting to complete wetting [5].

Often, the spreading parameter in Eq. (2.1) is defined in terms of the surface tension between the three interfaces; solid/liquid, solid/air and liquid/air as described first by Thomas Young (1773-1829) [2, 11]. At the interface between two different materials, for example two different liquids, surface tension is referred to as interfacial tension but the physics remain the same. Surface tension, as the name implies, arises due to the interactions of molecules at the surface, or at the interface in the case of interfacial tension. Liquid molecules in the bulk volume of the liquid have cohesive forces acting on all sides of the molecule which, when averaged, results in zero net force on the molecule. The molecules at the surface, however, have only the cohesive forces on the side of the molecule that is in contact with the bulk liquid. The half of the molecule that is in contact with the solid or gas boundary does not feel the cohesive forces and thus there is a net force acting on the molecule inwards towards the bulk of the liquid [6]. This is shown schematically in Fig. 2.3. If U is the energy per molecule in the bulk liquid, $U/2$ is roughly the energy of a molecule at the surface of the liquid since the molecule is in contact with about half the number of molecules compared to a molecule in the bulk [6]. If the molecule size is a^2 where a is the radius, we can then estimate the value of the the surface tension as,

$$\gamma \approx \frac{U}{2a^2}, \tag{2.2}$$

which is measured in J/m^2, energy per unit area, or equivalently N/m, force per unit length [6]. Surface tension is also temperature dependent. For example, water has a surface tension of 73 mN/m at 20°C and only 58 mN/m at 100°C [6].

There are many common examples of surface tension in nature. One such example is that of water striders "walking" on water. Although the striders are more dense than the water, they are able to walk upon the surface due to surface tension; the water does not wet their feet [6]. In addition, the fact that molecules do not like to be at the surface explains why liquids always act to minimize their surface area to volume ratio. This explains why drops and bubbles are spherical in shape when gravity is not a factor; the sphere shape minimizes the surface-to-volume ratio.

The spreading parameter can now be rewritten in terms of surface (interfacial) tension,

$$S = \gamma_{SG} - (\gamma_{SL} + \gamma_{LG}), \tag{2.3}$$

where γ_{LG} is the surface tension between the liquid and the air, γ_{SO} is the surface tension between the solid substrate and the air and γ_{SL} is the surface tension between the solid substrate and the liquid. Eq. 2.3 is depicted schematically in Fig. 2.2. As in Eq. 2.1, we can see that in Eq. 2.3 the system will adapt it's lowest energy configuration, or equivalently, minimize surface tension. Thus if the surface tension between the solid/air is larger than the sum of the solid/liquid tension and liquid/air tension, the liquid will spread.

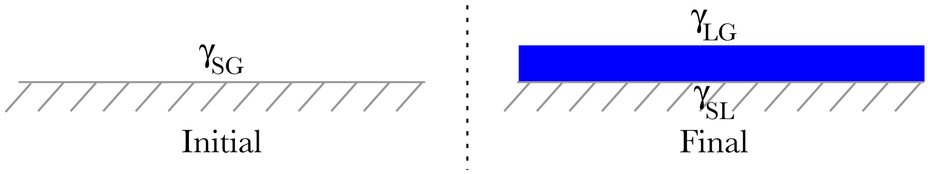

Figure 2.2:
Schematic of the different surface tensions involved in the spreading parameter defined by Eq. 2.3. In the initial picture on the left, the total surface energy is given by the surface tension between the solid/air interface. In the final picture on the right a thin liquid film is on the solid substrate and the total surface energy is given by the sum of the surface tension between liquid/air interface and solid/liquid interface. The spreading parameter is the difference in surface energy between the two cases depicted.

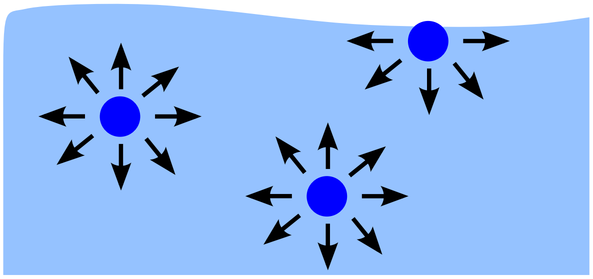

Figure 2.3:
Schematic of the forces acting on a molecule in the bulk of a liquid versus a molecule at the air/liquid surface.. The molecules in the bulk feel equal cohesive forces in all directions due to the other liquid molecules. The net force is zero. At the surface, however, the molecules feel a net force inward towards the bulk of the liquid, this inward force gives rise to the phenomenon known as surface tension [6].

If a liquid is not in the complete wetting regime, it will form a spherical cap on the surface if gravity effects are negligible. The equilibrium contact angle θ_E is determined by Young's relation (also known as the Young-Dupré relation), when the net force at the contact line is zero we have,

$$\gamma_{LG} cos\theta_E = \gamma_{SG} - \gamma_{SL}, \tag{2.4}$$

where the components of the surface tensions acting along the contact line have been balanced such that the liquid is not moving and the contact angle remains constant [2,6,11]. Eq. 2.4 is depicted schematically in Fig. 2.1.

The focus of this thesis is liquid droplets on thin films of identical liquid. We now know that if a liquid is on a solid the spreading parameter, S, dictates whether the liquid will wet the surface. This spreading parameter is determined by balancing the relevant surface tensions, as described by Eq. 2.3. In the case of a liquid drop on an identical liquid the situation become simpler. If the already present liquid film is stable, we know, simply due to the surface tension of the liquid/air boundary that the equilibrium configuration of the system is that of a flat liquid film. Surface tension acts to minimize the surface area to volume ratio and in the case of a drop on a film, the drop will level until the surface of the thin film becomes smooth. A flat, smooth liquid film minimizes the surface tension of the system. Intuitively, this makes sense,

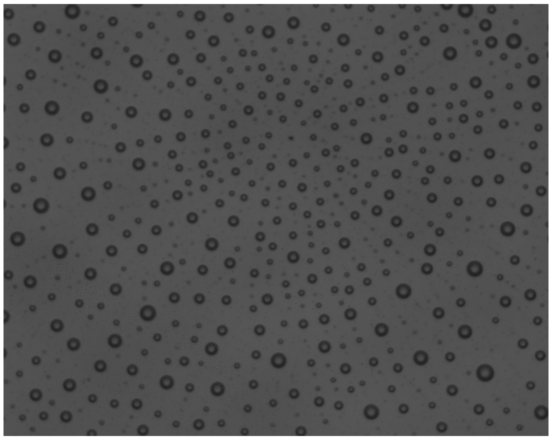

Figure 2.4:
Optical microscopy image of a ∼100 nm polystyrene film that has dewetted off a mica substrate. The field of view is ∼ 400 µm across.

as situations similar to this occur in everyday life. When a drop of honey falls back into the jar, the drop levels and the surface of the honey flattens. When rain falls on the ocean, the rain drops level and the ocean surface becomes smooth again.

The phenomenon of spreading occurs when a drop of liquid is incident on a surface such that the initial contact angle of the liquid is greater than the equilibrium contact angle. When the opposite case occurs, the drop will retract. In the extreme case, when the initial condition of the system is a flat liquid film and the equilibrium contact angle of the liquid is not zero ($S < 0$), a phenomenon known as dewetting can occur. Dewetting is the process by which a liquid film breaks up into holes. Over time the holes grow and merge with other holes. Eventually, the liquid film breaks up into droplets on the surface, this is shown in Fig. 2.4 which is an optical microscopy image of a polymer film dewetting off a mica substrate. A common example of dewetting in everyday life is that of a thin film of water dewetting off a freshly waxed car. The final contact angle that the droplets make with the substrate is dictated by Eq. 2.4.

There are two different mechanisms responsible for the dewetting process, spinodal and nucleation. In spinodal dewetting, the film is unstable and holes spontaneously form [6, 12–15]. Capillary waves arise due to thermal fluctuations in the film and are driven by long range van der Waals forces. These capillary waves grow in amplitude with a characteristic wavelength until the substrate is reached, at which point holes form [14, 15]. This process is analogous to phase separation in which the capillary waves are analogous to density fluctuations [14].

If nucleation is the mechanism for dewetting the film is said to be metastable [12]. In this case, the film can remain wetting the substrate unless there is a nucleation agent that lowers the energy barrier to dewetting. The specific nucleating agent can vary and can be dust on the substrate or a probe in contact with the film.

The thickness of the film determines if a film is unstable, stable, or metastable. Thick films, greater than a critical thickness, e_c, are stable and do not dewet. Films below this thickness dewet via one of the two methods described above. What dictates the stability of the film is the effective interface potential, ϕ which is a function of the film thickness e. The interface potential describes the excess free energy required to create surface as excess surface is required in the dewetting process [6, 15]. For stable films, the second derivative of the interface potential is positive ($\phi''(e) > 0$) . In unstable films, the second derivative of the interface potential is negative ($\phi''(e) < 0$) and in metastable films, there is an energy barrier to dewetting [15]. This is depicted in the schematic of Fig. 2.5 [15].

The critical thickness for dewetting, e_c, is related to a quantity known as the capillary length, κ^{-1}. The capillary length of a given fluid gives information as to whether gravity or surface tension forces will be driving system evolution. The hydrostatic pressure, P_g in a liquid at a given depth κ^{-1} is given by,

$$P_g = \rho g \kappa^{-1}, \tag{2.5}$$

where ρ is the density of the fluid and $g = 9.8$ m/s^2 is the Earth's gravity [6].

A curved interface creates a pressure known as the Laplace pressure. Gradients in Laplace pressure lead to fluid flow. We have already seen that gradients in curvature in a system are unfavourable due to surface tension. Laplace pressure is defined as the difference in hydrostatic pressure between the inside and outside of a bubble [6]. It is thus related to the curvature and also the surface tension through Laplace's theorem,

$$P_L = \gamma_{LG}\left(\frac{1}{R_1} + \frac{1}{R_2}\right) = \gamma_{LG} C, \tag{2.6}$$

where P_L is the Laplace pressure, R_1 and R_2 are the two principle radii of curvature of the bubble, C is the curvature and γ_{LG} is the surface tension between the liquid and the air [6]. The Laplace pressure is thus proportional to the surface tension and the capillary length through,

$$P_L \approx \frac{\gamma_{LG}}{\kappa^{-1}}. \tag{2.7}$$

If we compute Eq. 2.7 to Eq. 2.5 we obtain an expression for the capillary length,

$$\kappa^{-1} = \sqrt{\frac{\gamma_{LG}}{\rho g}}. \tag{2.8}$$

It is apparent that κ^{-1} is dependent on the properties of the liquid, specifically the density and surface tension [6]. When dealing with systems with radii greater than κ^{-1}, the effects of gravity become important, otherwise capillary forces are dominant and surface tension dictates the flow. In the work that is the focus of this thesis, the effects of gravity are negligible.

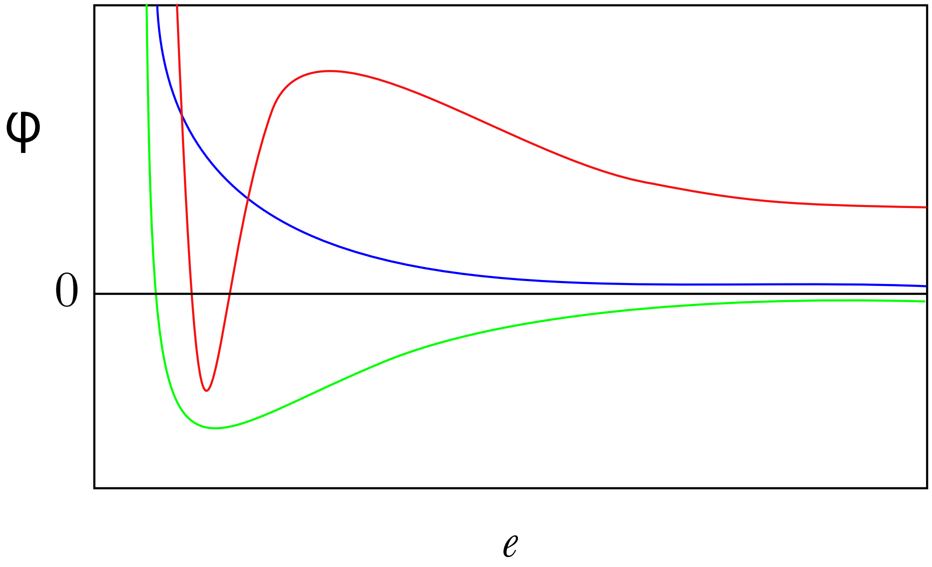

Figure 2.5:
Schematic of interfacial potential ϕ as a function of film thickness e for stable (blue), metastable (red) and unstable (green) films [15]. Stable films do not dewet, metastable films can dewet via nucleation and growth and unstable films spontaneously dewet via a spinodal process.

If gravity is the dominant force, the fluid film is thick and dewetting will be unfavourable. However, when surface tension dominates, dewetting will be favourable if the liquid does not wet the substrate. The critical thickness, e_c, is defined as,

$$e_c = 2\kappa^{-1} \sin\left(\frac{\theta_E}{2}\right), \tag{2.9}$$

where θ_E is the equilibrium contact angle described in Eq. 2.4 [6]. The thickness in Eq. 2.9 is the same as the equilibrium thickness of a puddle due to gravity and is obtained by minimizing the free energy of the system while invoking the assumption of constant volume [6]. Typically, e_c is on the order of a millimetre [12].

2.2 Lubrication Approximation

Understanding the flow behaviour of fluids is a difficult task. Unlike solids, fluid molecules have the ability to move independently of one another. Newton's second law, $\vec{f} = m\vec{a}$, takes the form,

$$\vec{f} = \rho\frac{d\vec{v}}{dt} \tag{2.10}$$

where $\vec{f}$ is the force on a specific fluid element, ρ is the mass of that element and $d\vec{v}/dt$ is the acceleration of the element. In general $\vec{f}$ is the sum of the driving force and force opposing the motion. In fluids the force opposing motion is the viscous force, this is analogous to friction opposing motion of solids. The driving force is a gradient in pressure, either hydrostatic or Laplace. To make the calculation easier we first assume incompressibility, $\Delta \cdot \vec{v} = 0$ which along with Eq. 2.10, leads to the Navier Stokes equation,

$$\vec{f}_D - \eta\Delta^2\vec{v} = \rho\frac{D\vec{v}}{Dt} \tag{2.11}$$

where $\vec{f}_D$ is the driving force for fluid flow, η is the viscosity, Δ^2 is the Laplacian operator, $\vec{v}$ is the velocity, ρ is the density of the fluid and $D\vec{v}/Dt$ is the material derivative of the velocity [6]. The Navier Stokes equation as written in Eq, 2.11 cannot be solved analytically and can only be solved numerically by inputting the proper initial conditions. Eq. 2.11 has widespread applications, such as predicting the weather forecast [16]. The fact that no analytical solution exists, due to non-linearity, explains why the weather forecast is often inaccurate. The proper initial conditions are required to accurately predict the weather. If the initial conditions are wrong the forecast will be wrong.

The difficulty in Eq. 2.11 arises for three reasons. First, there is an inertial term, $D\vec{v}/Dt \propto {v_{avg}}^2/L$ which makes the equation non-linear and gives rise to chaotic behaviour such as turbulence. Second, it is a three-dimensional vector equation and lastly, it is a second order differential equation [6]. However, when dealing with thin film flows, many of the problems in solving Eq. 2.11 can be eliminated using the lubrication approximation [6, 17–19]. First, we will define the Reynolds number, Re, which is the ratio between the inertial forces to viscous forces [1, 6],

$$\mathrm{Re} = \frac{\rho v_{avg}^2 L^2}{v_{avg} \eta L}, \tag{2.12}$$

where L is the characteristic linear dimension. If the Reynolds number is small (Re << 1) it is safe to neglect the non-viscous term in Eq. 2.11. That is to say that the overall velocity of the fluid is slow and the viscosity, η is the dominant means of flow. At the substrate, we invoked a no-slip boundary condition, meaning the velocity at the substrate is zero. Since the velocity gradient of the viscous fluid is continuous, and the film is thin, the overall velocity must be slow [6]. The low Reynolds number assumption is valid in thin film flows which means that only laminar flow is observed; turbulence is not an issue.

We can further simplify Eq. 2.11 by understanding the flow geometry of the system. Take for example a thin film that is standing vertically such that gravity dictates it flows downwards [6]. We know that the velocity at the substrate is zero as stated above and the velocity is continuous. We also know that the film supports an overall flow. Thus, we can say that there must be a flow gradient perpendicular to the substrate to produce overall flow parallel to the substrate [6]. This realization allows for the viscous force, which opposes flow, and the driving force to be decoupled as they act in directions perpendicular to one another.

We can, using the assumptions of the lubrication approximation as outlined above, simplify the non-linear, second order differential equation, Eq. 2.11 to the much simpler,

$$f_{Dx} - \eta \frac{\partial^2 v}{\partial z^2} = 0 \tag{2.13}$$

which is solvable by integrating twice with respect to z [6]. It is important to note that Eq. 2.13 is written for the geometry of a thin film flowing in one direction, x, with a gradient perpendicular to the substrate in the z-direction, but this is not necessary. The lubrication approximation can be rewritten for a number of different geometries and driving forces [17–20].

We can determine the flow profile of a thin film by solving Eq. 2.13. If we integrate twice with respect to z we obtain,

$$v(z) = \frac{z^2 f_{Dx}}{2\eta} + c_1 z + c_2, \tag{2.14}$$

where c_1 and c_2 are the constants of integration. The first boundary condition of the system requires that the velocity of the fluid at the substrate be zero ($v = 0$ at $z = 0$) which leads to $c_2 = 0$. The second boundary states that the velocity of the fluid at the liquid-air boundary must be continuous, $\partial v/\partial z = 0$ at $z = e$, where e is the thickness of the film. This condition is based on the observation that an air boundary cannot withstand any viscous stress as there is nothing in the air that will be able to balance the excess force [6]. This condition leads to $c_1 = -f_{Dx}e^2/\eta$. We now have,

$$v(z) = \frac{f_{Dx} z^2}{2\eta} - \frac{f_{Dx} e z}{\eta}, \tag{2.15}$$

where it is now clear that the velocity gradient perpendicular to the substrate has a parabolic profile, this is known as Poiseuille flow and is shown schematically in Fig. 2.6 [6].

We can obtain an expression for the average velocity of a thin film,

$$v_{avg} = \frac{1}{e}\int_0^e v(z), \tag{2.16}$$

where $v(z)$ is given by Eq. 2.15. If we compute the integral in Eq. 2.16, we find,

$$v_{avg} = -e^2 f_{Dx}/3\eta. \tag{2.17}$$

The rate of flow Q is given by ev_{avg},

$$Q = -e^3/3\eta f_{Dx}. \tag{2.18}$$

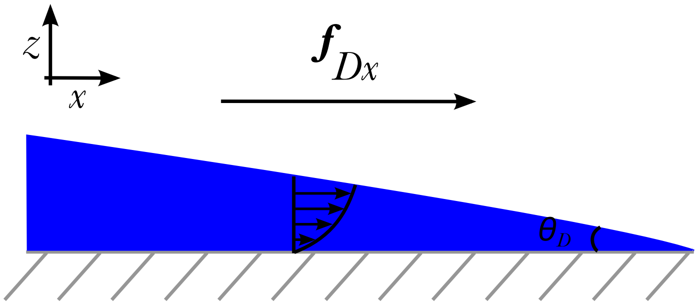

Figure 2.6:
Schematic of the Poiseuille flow profile in thin film flows due to a due to a driving force f_{Dx}. The gradient in velocity is in the z direction and the overall flow is in the x direction. The pressure in the thin film is highest on the left of the schematic and lowest on the right; fluids always flow from regions of high pressure to low pressure. The fluid will continue to flow until the equilibrium flat film configuration is achieved.

We can see in Eq. 2.18, that if a film is twice as thick, it will support eight times the rate of flow. We can also see in Eq. 2.17 that the velocity is inversely proportional to the viscosity of the fluid and directly proportional to the driving force which makes sense intuitively.

A common approach to understanding thin film flow is to use scaling laws to gain intuitive understanding to the evolution of the system. While the details of the flow may be lost, the fundamental physics remain and in practice many systems are not as easy to solve explicitly [6].

In this discussion of the lubrication approximation we have not yet defined the driving force for fluid flow, $\vec{f_D}$. Fluids flow due to gradients in pressure, either hydrostatic or Laplace. Either gravity is causing the fluid to flow downward, a gradient in Laplace pressure is causing the film to level in some way, or some combination of the two. Whether it is gravity or Laplace pressure driving fluid flow, $\vec{f_D} = -\nabla P$. In this thesis project we are dealing with systems that are dominated by surface tension; Laplace pressure is the driving force, and gravity can be neglected.

2.2.1 Example: Horizontal Levelling

To demonstrate the usefulness of the lubrication approximation, a simple example of a thin film levelling due to surface tension will be presented as outlined in the book, "Capillarity and Wetting Phenomena: Drops, Bubbles, Pearls and Waves" by Pierre-Gilles de Gennes, François Brochard-Wyart and David Quéré [6]. This example is relevant to the focus of this thesis which deals with the levelling of spherical caps on thin films. In this example, a thin film with wavelength λ will level due to a gradient in Laplace pressure. This system is shown schematically in Fig. 2.7. For the lubrication approximation, we must have the condition that the relevant lateral direction be much larger than the horizontal direction; the wavelength of the perturbation in the film must be much greater than the height of the film ($\lambda >> e$).

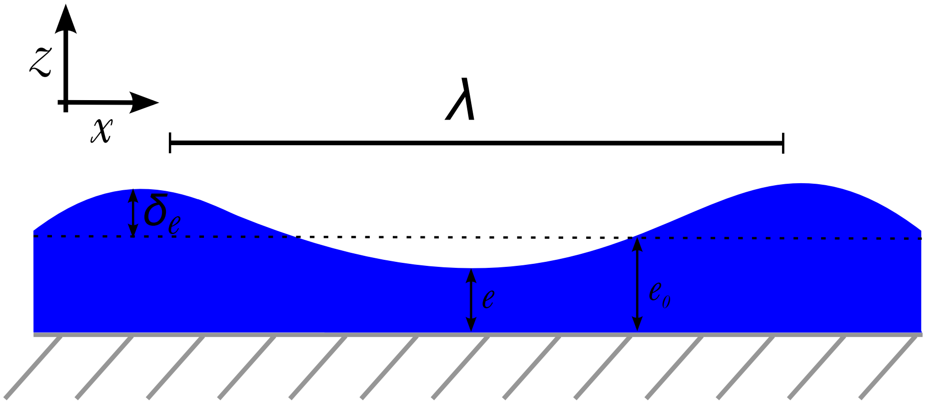

Figure 2.7:
Schematic of a thin film with equilibrium height e_0, minimum height e and deviation from equilibrium δe, with wavelength $\lambda >> e$. The pressure difference (Laplace or hydrostatic) in the film will drive the system to equilibrium which, in this case, is a flat film of height e_0. The rate of film levelling can be determined with the lubrication approximation.

We are interested in the characteristic timescale of levelling of the film shown in Fig. 2.7. The height of the film varies as a function of x as,

$$e(x) = e_0 + \delta_e cos(qx), \tag{2.19}$$

where e_0 is the initial height of the film, δ_e is the perturbation in the height and q is the wavevector, $q = 2\pi/\lambda$. As stated above, the driving force for levelling that we are concerned with is Laplace pressure. We can compute the capillary length to determine if gravity or Laplace pressure is dominating flow. The hydrostatic pressure is given by the difference in height between a crest and a trough, shown in Fig. 2.7,

$$P_g \propto \rho g \delta_e, \tag{2.20}$$

where P_g is the pressure in the system due to gravity. The Laplace pressure is related to the surface tension and the curvature (second derivative with respect to x of Eq. 2.19),

$$P_L \propto \frac{\gamma_{LG}\delta_e}{\lambda^2}. \tag{2.21}$$

The ratio between Eq. 2.20 and Eq. 2.21 is the capillary length, κ^{-1} described by Eq. 2.8. When κ^{-1} is larger than the wavelength of disturbance, Laplace pressure dominates, when the opposite is true, gravity dominates.

When the Laplace pressure dominates, the driving force for flow is the gradient in pressure, $\partial P_L/\partial x$. Thus, from Eq. 2.18,

$$Q = \frac{\gamma_{LG}e^3}{3\eta}\frac{\partial^3 e}{\partial x^3}. \tag{2.22}$$

Using Eq. 2.19 along with the assumption that $\delta_e << e$ we obtain,

$$Q = \frac{\gamma_{LG}e_0^3\delta_e q^3 \sin(qx)}{3\eta}. \tag{2.23}$$

We also assume the volume of the system is conserved,

$$\frac{\partial Q}{\partial x} = \frac{-\partial \delta_e}{\partial t}, \tag{2.24}$$

where the right side of Eq. 2.24 describes the decrease of the amplitude of the disturbance with time and the left side describes the change in the flow rate with time. Using Eq. 2.24 and the derivative of Eq. 2.23 we obtain,

$$\frac{e_0^3}{3\eta}\gamma_{LG}\delta_e q^4 \cos(qx) = -\frac{\partial \delta_e}{\partial t}. \tag{2.25}$$

Lastly, if we take the integral of both sides of Eq. 2.25 we obtain,

$$\frac{e_0^3}{3\eta}\gamma_{LG}\delta_e q^4 \cos(qx)t = \delta_e, \tag{2.26}$$

where we are now in a position to determine the characteristic levelling time, τ of the film. Using Eq. 2.26 we find this characteristic levelling time is given by,

$$\tau = \frac{3\eta}{e_o^3 \gamma_{LG} q^4}, \tag{2.27}$$

where it is clear the film follows an exponential relaxation behaviour with λ; $\lambda \propto 1/q$ [6].

2.3 Tanner's Law

As discussed in Section 2.1, the spreading parameter, S, dictates whether a liquid will wet a surface. If the equilibrium contact angle of a liquid on a surface is zero, that is to say the liquid will completely wet the surface and the droplet is small such that gravity can be neglected ($R < \kappa^{-1}$), the droplet will spread according to Tanner's law (also known as the Tanner-Voinov-Hoffman relation) [21–23]. Over three decades ago, in 1979, Tanner published a paper [21] providing both experimental results and a theoretical framework describing the spreading of a liquid drop on a solid surface. It was found that the droplet radius, a, decreased in time, t, as,

$$a(t) \approx t^{1/10}. \tag{2.28}$$

Tanner's law has been observed experimentally [24–27] and confirmed theoretically and computationally [28, 29] by many different research groups in the three decades since Tanner first published his results.

2.3.1 Derivation of Tanner's Law

The theoretical framework provided by Tanner was based on the lubrication approximation for thin film flows as described in Section 2.2 as well as volume conservation and self-similarity of the profiles. Self-similarity is when all the droplet profiles at different times in the experiment can be rescaled such that all the data falls on the same profile. This self-similarity is proven by non-dimensionalising the variables as described by Tanner [21]. Tanner assumed that the slope of the profile at the inflection point evolves in time as t^{-n}, which leads to the scaling in Eq. 2.28.

The derivation that will be presented here was adapted from [6] and is based on viscous dissipation at the contact line. First we will investigate the behaviour of a spreading wedge of liquid on a wetting substrate as seen in Fig. 2.6. If we assume that the angle θ is small, the slope of the wedge in Fig. 2.6 is $\tan\theta \approx \theta$. The contact line is moving such that the slope remains constant and the dynamic contact angle θ_D is larger than the equilibrium contact angle θ_E defined in Eq. 2.4 [6]. In the z-direction, perpendicular to the substrate, there is a velocity gradient as defined by Poiseuille flow. The velocity gradient is obtained by taking the derivative with respect to z of Eq. 2.15,

$$\frac{d\vec{v}}{dz} \approx \frac{3v_{avg}}{\theta_D x}, \tag{2.29}$$

where we have used the fact that at the surface $z = e = \theta_D x$.

As the wedge moves along the substrate in the x direction, energy is dissipated. This energy dissipation, which is given by the product of the rate of change of entropy, $\dot{S}$, and temperature, T, is given by,

$$T\dot{S} = \int_0^\infty dx \int_0^e \eta \left(\frac{d\vec{v}}{dz}\right)^2 dz \cong \frac{3\eta {v_{avg}}^2}{\theta_D}, \int_0^\infty \frac{dx}{x}, \tag{2.30}$$

where the $T\dot{S}$ is the energy dissipated per unit length and Eq. 2.29 is substituted to obtain the final expression. To avoid the divergence of the integral in Eq. 2.30 we integrate from the molecule size a to the length of the system L,

$$\int_a^L \frac{dx}{x} = ln\left(\frac{L}{a}\right) \equiv l, \tag{2.31}$$

where the dimensionless coefficient l takes values between 15 and 20 [6].

The rate at which work is done by the driving force F is equivalent to the viscous energy dissipation,

$$T\dot{S} = Fv_{avg}, \tag{2.32}$$

where F is the driving force related to Eq. 2.4, and v_{avg} is the average velocity of the profile which is also the velocity of the contact line [6]. At θ_E the net force is zero (Eq. 2.4), at θ_D we have,

$$F(\theta_D) = \gamma_{SG} - \gamma_{SL} - \gamma_{LG}cos(\theta_D), \tag{2.33}$$

which is clear when examining the forces in Fig. 2.1.

We are now in a position to derive Tanner's law. First, we know the driving force for spreading is given by Eq. 2.33 above. However, the universality of Tanner's law indicates that the spreading behaviour is independent of S as long as the fluid completely wets the substrate ($S > 0$). The explanation for this is that a very thin precursor film emerges around the circumference and acts to dissipate the excess surface energy, this precursor is depicted schematically in Fig. 2.8. The precursor film is explored in Section 2.3.2. The net force responsible for spreading is thus given by the sum of the force of traction in the drop (given by Eq. 2.33 with $\gamma_{SG} = 0$), and the forces in the flat film (given by $\gamma_{SL} + \gamma_{LG}$),

$$F = \gamma_{LG} - \gamma_{LG} cos\theta_D \cong \gamma_{LG}\frac{\theta_D^2}{2}, \tag{2.34}$$

where we have invoked the small angle approximation that is valid in the regimes where Tanner's law holds. Second, we assume volume conservation and that the drop is a spherical cap,

$$V = \frac{\pi}{4}a^3\theta_D. \tag{2.35}$$

where V is the volume and a is the radius of the spherical cap shown in Fig. 2.8 [2,6]. We know that the velocity of spreading is the rate of change of a and using Eq. 2.30, Eq. 2.32 and Eq. 2.34 we obtain,

$$v = \frac{da}{dt} = \frac{\theta_D}{3l\eta}F = \frac{\gamma\theta_D^3}{6l\eta}. \tag{2.36}$$

If we then take the time derivative of Eq. 2.35 and substitute Eq. 2.36 and Eq. 2.35 back in again we obtain,

$$\frac{\gamma}{2l\eta}\left(\frac{4V}{\pi}\right)^{1/3} dt = -\frac{d\theta_D}{\theta_D^{13/3}}. \tag{2.37}$$

Integration of of Eq. 2.37 and omitting numerical coefficients leads to the scaling relation,

$$\theta_D(t) \approx t^{-3/10}, \tag{2.38}$$

which is Tanner's law and can be rewritten as $a(t) \approx t^{1/10}$ or $d(t) \approx t^{-1/5}$ using the

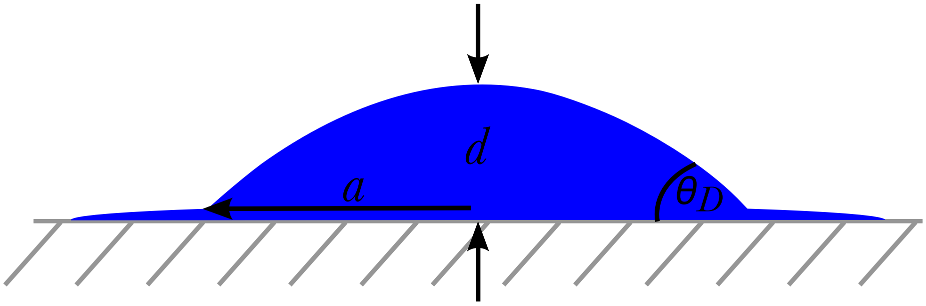

Figure 2.8:
Schematic of a droplet on a wetting substrate with radius a, height d and dynamic contact angle θ_D. A precursor around the circumference of the drop is visible and effectively absorbs the excess surface energy between the liquid and the solid substrate

equations for the volume of a spherical cap.

2.3.2 Precursor Film

Remarkably, Tanner's law is independent of the spreading parameter S, given that $S > 0$. That is to say that the liquid and solid surface interactions do not change the spreading law that is observed. This result is explained by the presence of a precursor layer that develops around the circumference of the droplet as mentioned briefly in the derivation of Section 2.3.1. This precursor layer, as depicted schematically in Fig. 2.8 is a thin, wedge-like film that effectively dissipates the excess surface energy between the liquid and the solid and has a thickness on the order of 0.1 nm to 10 nm [2, 4, 8, 30, 31]. This precursor was first observed by Hardy in 1919 through a clever experiment [32]. Hardy observed that a thin rod would roll when the spreading front approached the rod, but before the contact line of the spreading front actually contacted the rod. This implied that the friction of the surface was reduced pointing to the existence of a wetting layer; the precursor [32]. This has been experimentally verified since Hardy's discovery many times [30, 31, 33–36] and observed in computer simulations [29, 37–39].

To verify that Tanner's law is independent of the energy of the spreading surface, as long as the liquid is in the total wetting regime, the spreading behaviour of silicone oil on two different energy surfaces was observed [40]. In one case, silicone oil was observed spreading on a clean silicon wafer, with a large positive S [40]. In a second case, a grafted surface of octadecyltrichlorosilane with smaller S value than the clean silicon wafer was used [40]. Even though the energy of the grafted wafer was less than the clean wafer, the spreading parameter was still positive, and the silicone oil still wet the surface completely. The spreading of the bulk droplet was observed to be independent of S and the identical Tanner's law spreading behaviour was observed on both surfaces [40].

One of the initial problems in the theoretical description of droplets spreading is the no-slip boundary condition. This condition, as described in the lubrication approximation of Section 2.2, gives rise to Poiseuille flow that is characteristic of thin film flow and is invoked in the theoretical description of Tanner's law. It is clear, however, that this condition must be violated in the spreading of drops as the velocity at the substrate cannot be strictly zero or spreading would never be observed. The presence of a precursor film allows this condition to hold as it is only the precursor film that violates the no-slip boundary. The bulk of the drop is spreading on a thin film of identical fluid and in the bulk a Poiseuille flow profile is valid [36].

The precursor film formation and spreading does not follow Tanner's law and is driven by long range van der Waals forces [2,31,36,41]. In fact, the shape and speed of the spreading of the precursor film is dictated by S [36,40]. The precursor film forms through two different mechanisms [36]. The initial stages of precursor formation are fast and referred to as "adiabatic". In the adiabatic stage, the precursor forms much faster than the bulk drop spreads. The spreading velocity around the circumference is constant in this early regime [31, 36]. In the later time, the diffusive spreading regime dominates which is driven by a balance between van der Waals forces and viscosity. In this diffusive regime, the length of the precursor film, as measured from the inflection point, to the point where the thickness goes to zero scales with time as $t^{1/2}$ [36].

The presence of a precursor film essentially means the bulk of the droplet is spreading on a thin film. This realization is relevant to the focus of this thesis; liquid droplets levelling on thin films of identical liquids. If a drop is spreading on a thin film that is equivalent in height to the precursor film, Tanner's law should be recovered. This situation, with a pre-existing precursor film has been studied computationally on two-dimensional droplet systems [42].

2.4 Past Spreading Experiments

Tanner's law is observed when a droplet is spreading on a wetting substrate, Laplace pressure is dominating flow in the bulk of the droplet, the fluid is viscous and non-volatile and the small angle approximation for the contact angle is valid. When these relatively restrictive constraints are not met, deviations from Tanner's law are observed. In this section a brief discussion on the literature available describing systems for which Tanner's law is not observed will be presented.

The initial stages of droplet spreading, when the drop is first incident on the surface do not follow Tanner's law. The small angle approximation is violated and inertia plays a role in the dynamics of spreading [9, 43, 44]. Similarly, late stage spreading dynamics can deviate from Tanner's law [45]. Instead of forming a thin liquid film as predicted by Tanner's law the equilibrium configuration of the droplet in certain cases can take a pancake geometry [2]. This geometry has also been predicted theoretically [45]. For liquid crystal spreading, the late time dynamics are predicted to speed up in comparison to Tanner's law [45].

When the droplets are large, the driving force for spreading becomes gravity and the droplets spread with a larger time dependence than Tanner's law [46]. In this gravity regime, if the drop is spreading on a completely wetting substrate ($S > 0$), the droplet radius grows like $a \approx t^{1/7}$ [8, 46]. The shape of the droplet becomes more "pancake" than spherical cap [8, 46]. As in the divergence from Tanner's law when drops are large, when drops are very small a divergence also occurs [34]. In particular, for very small drops, the driving force becomes the van der Waals interactions as in the precursor spreading, this has been observed experimentally and theoretically and the spreading is faster than Tanner's law [34].

Tanner's law requires the spreading fluid be Newtonian, non-volatile and viscous. Deviations from these requirements change the spreading dynamics. For example, if the fluid is shear-thinning, the no-slip boundary condition is not a problem and it has been predicted and observed that the rate of spreading is less than Tanner's law [47–49]. For shear thickening fluids however, the rate of spreading is predicted to be faster [48]. It has also been predicted that thermal fluctuations can create faster spreading rates [50]. One interesting spreading experiment involved ordered lamella diblock co-polymers [35]. When the diblocks are ordered, the droplet becomes conical in shape and the rate of spreading is reduced compared to Tanner's law [35]. The shape of droplet effects the spreading. For example, if an electric field is applied to a drop it becomes conical and the power law spreading behaviour changes [9].

Liquid droplets have also been observed spreading on various liquid substrates. In the case when the two liquids are not identical and immiscible, the droplet does not take on the characteristic spherical cap shape that droplets on solids take but rather a lens geometry [51, 52]. Take for example the case of a viscous drop of poly(dimethylsiloxane) (PDMS) on a mixture of glycerol and water which is less viscous [51]. In this case, if the driving force is capillarity, the droplet radius spreads like $t^{1/4}$, according to lubrication approximation. If gravity is the dominant driving force for spreading on a liquid, the radius is predicted to increase with time as $t^{1/2}$ [52]. Both the gravity and the capillary regimes have been verified experimentally [51]. The rate of spreading of liquids on liquids is faster than the equivalent spreading on a solid [51,53].

In addition to the physics of spreading, when a liquid is on a porous substrate, the liquid will simultaneously spread and interpenetrate the substrate film [9,54–57]. One such example is that of a liquid polymer drop spreading on a liquid polymer film of different molecular weight. Molecular dynamics simulations investigated the difference between polymer droplets spreading on glassy polymer films vs liquid polymer films [55]. In the glassy case, the substrate behaves as a solid and a precursor foot is observed, in the liquid substrate case the polymer interpenetrates the film and no precursor is observed [55].

2.5 Polymers

The materials used to observe liquids levelling in this research are linear homopolymer systems. While the physics of liquids spreading are general and not specific to polymeric systems, polymers are an ideal system experimentally for a number of reasons which are outlined below.

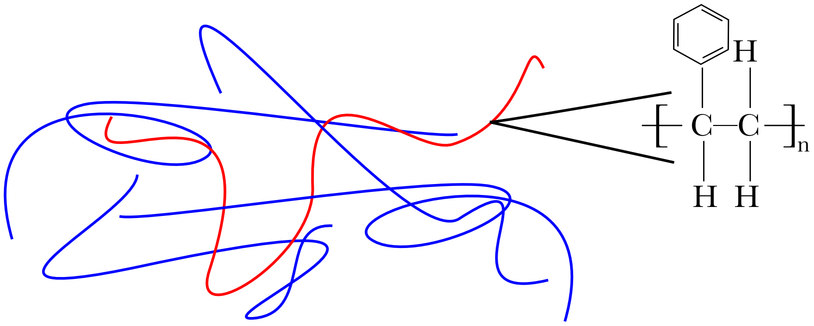

Figure 2.9:
Schematic of a polymer melt with many polymer chains (red and blue). The monomer unit is this case is a styrene monomer shown in brackets. Many styrene monomers covalently linked create the polymer polystyrene.

Polymers are long chains of repeating monomer units that have been covalently linked together as shown schematically in Fig. 2.9. The monomer unit can vary drastically from polymer to polymer and will dictate the properties of the polymer; the monomer unit shown in Fig. 2.9 is styrene. Common examples of polymers include plastics, DNA and many coatings. The length of the polymer chains can also dictate the properties of the polymer system, specifically the viscosity [6]. Chemists have the ability to control the length of the chains with a high degree of precision. Polymer systems are ideal work with experimentally due to this high degree of controllability [6]. Polymers are also are non-volatile due to the high mass of the individual molecules. Polymer systems have low surface tension which means they do not generally self-contaminate [6].

The molecular weight, M_w of a linear polymer chain can be thought of as the length of the polymer. Molecular weight is directly related to the viscosity of the polymer molecules; as the chains get longer the viscosity increases. The scaling relationship between M_w and viscosity, η is given by,

$$\eta \sim M_w^{\nu}, \tag{2.39}$$

where the exponent $\nu \sim 1$ for a M_w below a critical M_w known as the entanglement molecular weight, M_e, and $\nu \sim 3.4$ above M_e [58]. This has been experimentally verified for a wide variety to polymeric systems [58].

Viscosity is also related to temperature through the empirical Vogel-Fulcher law,

$$\eta(T) = \eta_0 \exp \frac{T_A}{T - T_V}, \tag{2.40}$$

where η_0 is a pre-factor, T_A is the activation temperature, T is the temperature and T_V is the Vogel temperature [59]. As is clear in Eq. 2.40, the viscosity diverges at T_V. Due to this divergence, viscosities near T_V cannot be measured experimentally. In fact, the temperature below which the viscosity cannot be measured is known as the glass transition temperature, T_g, and is typically 50K above T_V [59]. Below T_g, the viscosity of the system is so large that the system is considered a solid (glass) which is why it is referred to as the glass transition.

Equivalent to the Vogel-Fulcher law is the Williams-Landal-Ferry (WLF) equation,

$$\log(a_T) = -\frac{C_1(T - T_g)}{C_2 + (T - T_g)}, \tag{2.41}$$

where a_T is a shift factor, C_1 is a constant which has values ranging from 14-18 and C_2 is a constant with values ranging form 30-70K [59, 60]. The shift factor a_T is related to viscosity by the following relation,

$$a_T = \frac{\eta(T)}{\eta(T_g)}, \tag{2.42}$$

where the reference temperature is typically T_g but this is not necessary [59].

The shift factor a_T refers to the shift related to time-temperature superposition. Simply by changing the temperature of a polymeric system, different time-scale behaviours can be observed (i.e. different viscosity) [59]. Thus, by observing the behaviour of the system over a wide range of temperatures, a master curve can be obtained by shifting the data by a_T. Examples of where the time-temperature superposition holds includes creep compliance and tensile modulus [59]. Creep compliance refers to how much a material moves when a stress is applied. The hotter the material; the greater the creep. If creep were to be observed over a very long period of time (∼20 orders of magnitude) at one temperature, a master creep curve would be observed as is shown schematically in Fig. 2.10 [59]. However, experimentally, observing a system for ∼20 orders of magnitude in time is almost impossible. By varying

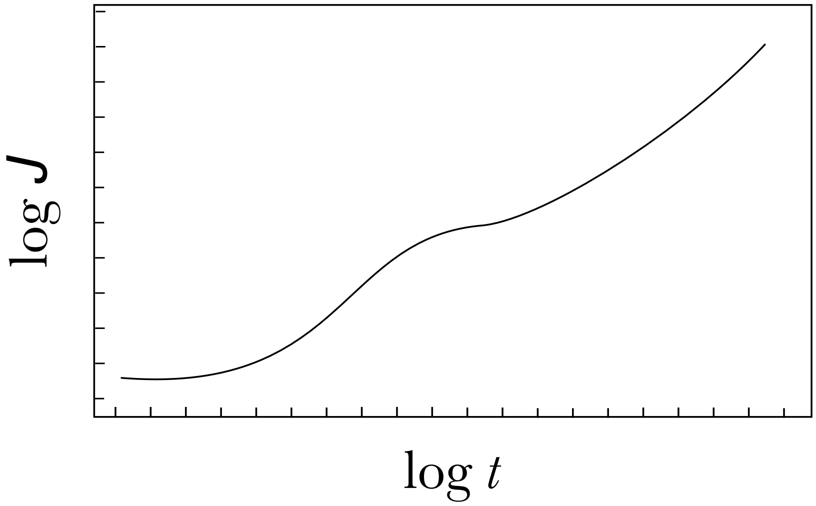

Figure 2.10:
Schematic curve of the creep compliance of polystyrene as a function of rescaled time. Experimentally, curves such as this are obtained using time-temperature superposition [59].

temperature, all portions of the master creep curve can be observed in experimentally accessible times and by shifting the data by a_T, the master curve can be constructed.

At the glass transition temperature T_g, the viscosity of the polymer system goes to infinity and cannot be measured. At this temperature the system becomes glassy, and the polymer molecules are frozen in place. One of the nice properties of some polymers is that this T_g is easily accessible experimentally. This means that by simply varying the temperature, not only can the viscosity of the system be precisely controlled, the system can either be in the liquid state or in the solid glassy state.

The ability to control the viscosity of the system by varying M_w or temperature is attractive experimentally because it allows the timescale of the experiment to be controlled and even frozen by quenching below T_g. This allows for precise study of polymer dynamics. Other simple fluids do not have the same controllability with viscosity which makes observing fast time or slow time dynamics difficult.

2.6 Instrumentation

2.6.1 Atomic Force Microscopy

An atomic force microscope (AFM) is used to view topological features, on the order of 0.1 nm, with a high precision. This type of resolution is not possible using an optical microscope as the resolution of optical microscopy is limited to the wavelength of visible light (on the order of 100 nm).

An AFM works by scanning the surface of a sample. An analogous macroscopic example of an AFM is a record player. Much like a record player, an AFM has a arm, known as a cantilever, with a small, sharp tip at the end. The AFM tip has a diameter of approximately 10 nm and is a few microns in length [61]. The cantilever is on the order of 100 µm in length [61]. The tip scans the surface of the substrate, much like the needle on the record player scans the record for indents and waves to produce sound. The AFM monitors the position of the cantilever and tip using one of two imaging methods to produce a scan of the surface. The two imaging methods are known as contact and non-contact mode. In this thesis, non-contact mode is used to determine the profile of the polymer droplets and is described below.

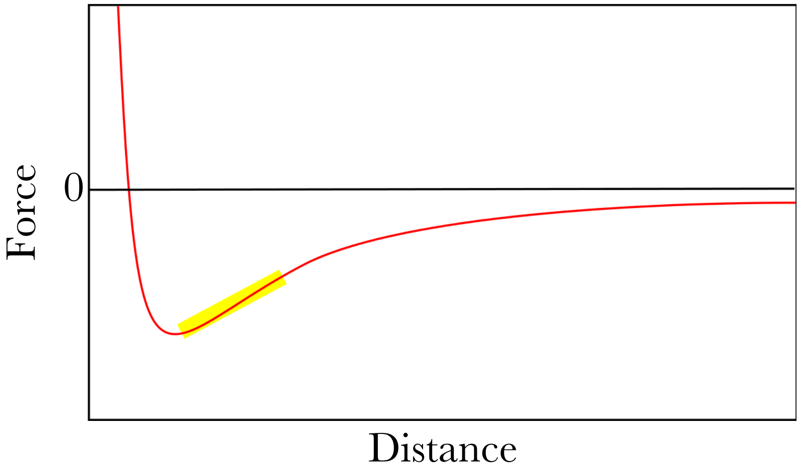

Figure 2.11:
Schematic of the Lennard-Jones potential showing force as a function of distance to a sample. In non-contact mode the force between AFM tip and sample is attractive and the distance for which non-contact mode operates is highlighted in yellow [61].

In non-contact tapping mode, the AFM tip very gently "taps" the sample. In this tapping mode the topography of the sample is determined by monitoring the oscillation of the AFM tip. The tip is set to oscillate at a frequency that is slightly higher than it's resonant frequency with an amplitude on the order of 10 nanometers [61]. When near the surface of the sample, attractive van der Waals forces become important and the amplitude of the tip oscillation is changed. The ideal distance for tapping mode is given by the Lennard-Jones potential and is shown schematically in Fig. 2.11. The idea of tapping mode AFM is to keep amplitude of oscillation constant. When the tip moves too far away from the sample, the amplitude of oscillation increases due to the absence of van der Waals forces. When the tip moves too close to the sample, the amplitude of oscillation is decreased. In order to monitor precisely the oscillation of the tip, a laser is pointed at the tip, reflected and monitored using a photodiode. The photodiode is coupled to a feedback piezoelectric transducer that moves the tip up or down in order to maintain a constant oscillation frequency. A schematic of an AFM is shown in Fig. 2.12. The amount the tip must move up or down to maintain the constant oscillation amplitude determines the topography of the sample as the tip scans horizontally [61].

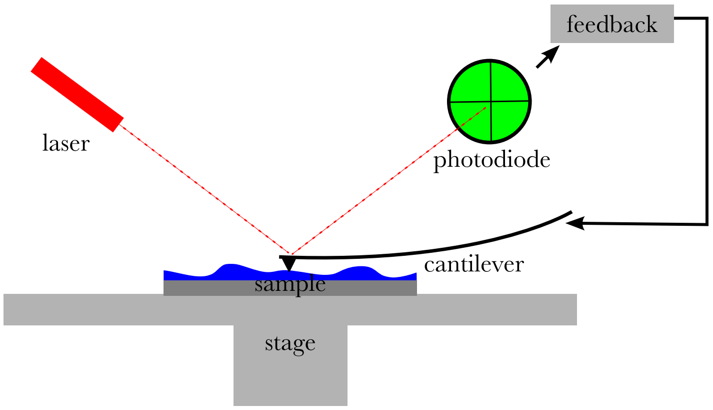

Figure 2.12:
Schematic of an AFM with the different components. The laser is reflected off the cantilever tip and the position recorded with a photodiode. A feedback mechanism ensures the oscillation amplitude of the tip is constant by moving the cantilever up or down vertically. In this manner the cantilever tip scans the surface of a sample and determines the topography of the surface.

2.6.2 Ellipsometry

An ellipsometer is an optical tool that can precisely measure the thickness of thin films, with precision on the order of 0.1 nm, as well as the refractive index given that the films are homogeneous and isotropic, meaning they are flat in the region of interest [62]. Films that are not homogeneous can also be measured but will not be discussed in the context of this thesis.

In order to understand the principles of ellipsometry, we must first discuss the polarization of light. When an electromagnetic wave is travelling in some direction, the electric and magnetic field components of the wave are orthogonal to the direction of motion. If the electric field has a specific orientation as the wave propagates it is said to be polarized [62]. For example, linearly polarized light occurs when the two wave components are completely in phase. When this is the case the electric field vector traces a line in space, hence it is linearly polarized. Circularly polarized light is obtained when the electric field vector draws a circular path as the wave propagates. Similarly, elliptically polarized light is obtained when the electric field vector draws an elliptical path as it propagates.

Polarization of light can be affected by passing through polarization filters such as polarizers and quarter wave plates. Polarization is also affected when it passes through different, non-metallic materials. The change in polarization upon reflection and refraction depends on both the angle of incidence and the properties of the material, specifically the refractive index, n and the distance the light travels through the material; the material thickness t [62].

An ellipsometer works by measuring how the polarization of light changes when it passes through a given sample. First, a laser beam is passed through a polarizer, which is a filter, that has been rotated to a specific angle P. The light entering the polarizer is circularly polarized and exits the polarizer linearly polarized [63]. This linearly polarized light is then passed through a quarter wave plate and becomes elliptically polarized. The elliptically polarized is incident on the sample and upon reflection is linearly polarized. Lastly, this linearly polarized light is passed through another polarizer, called the analyzer at some angle A such that the null condition is obtained [63]. At null, all light is extinguished and no light reaches the detector. The angles A and P are unique. Using the equations of ellipsometry which are explained elsewhere [62] and an initial guess of the index of refraction, n and thickness, t, the two quantities may be determined with a high degree of precision.

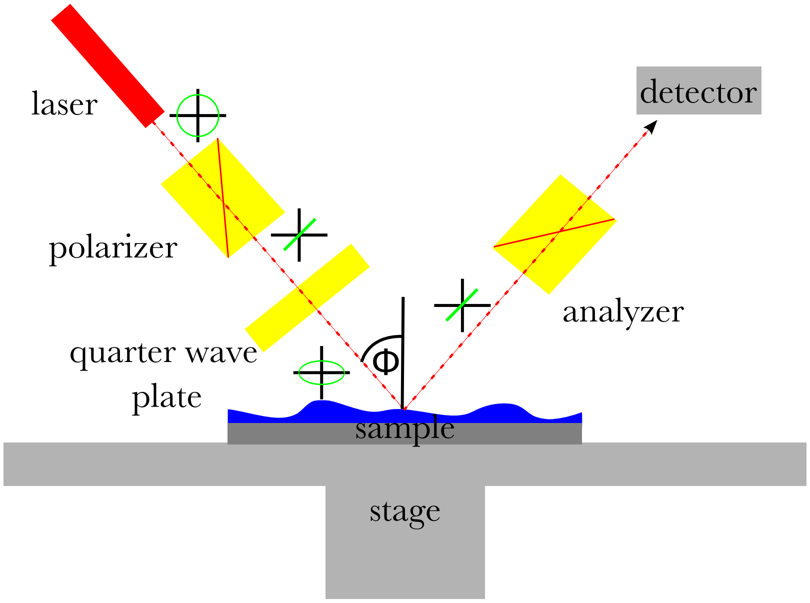

Figure 2.13:
Schematic of an ellipsometer. First circularly polarized light becomes linearly polarized by passing through a polarized at angle P. This light becomes elliptically polarized by passing through a quarter wave plate and is incident on the sample. Upon reflection, the light is linearly polarized and passes through the analyzer rotated to angle A such that all light is extinguished; this is the null condition.

Chapter 3

Experimental Procedure

3.1 Sample Preparation

3.1.1 Polystyrene

To study liquid droplets spreading on thin films of identical liquid we have developed a method of sample preparation using spincasting, dewetting and floating. The ideal sample geometry is that of a perfect spherical cap atop a thin film of identical material (see Fig. 3.1). Preparing a sample such that the initial conditions are well controlled and easily varied is not trivial and may point to why such a system has not, to our knowledge, been studied experimentally in the past. Specifically, we wish to control the aspect ratio of droplet height d_0, to underlying film height e; d_0/e. Here, well controlled samples with the desired geometry have been fabricated using the polymer polystyrene (PS) with weight averaged molecular weight, $M_w = 118$ kg/mol and a polydispersity index of 1.05 (Polymer Source Inc., Canada). First, PS is dissolved in the solvent toluene with solutions ranging from 0.5 % to 10 % by weight. Toluene is a good solvent for PS. A thin film of PS is spincast onto a clean 10×10 mm^2 Si substrate. The film thickness is controlled precisely by varying the spin speed as well as the concentration of the PS solution. The thickness was determined using an imaging ellipsometer (EP3, Accurion, Germany). By making films in this manner we obtained film thicknesses ranging from 50 nm to 1000 nm.

We fabricated thicker films of $\sim$ 2000 nm using a floating technique as spinning films greater than 1000 nm is difficult. Films of $\sim$500 nm were first spincast onto a

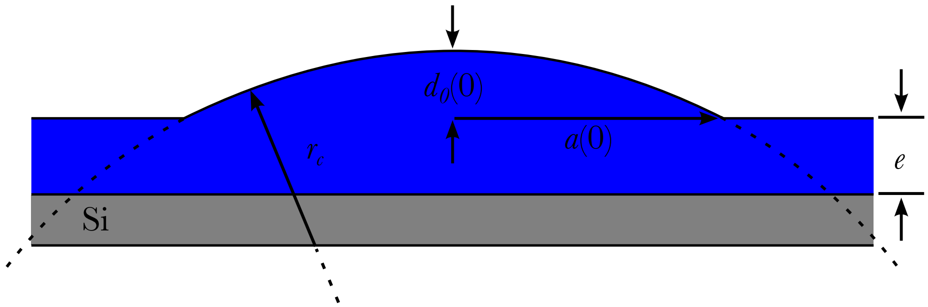

Figure 3.1:
Schematic showing a perfect spherical PS cap before heating is observed (t=0), of radius $a(0)$, height $d_0(0)$ and radius of curvature r_c atop a thin PS film of height e. The system is on a silicon substrate.

mica substrate and subsequently floated onto clean water (Milli Q, 18.2 MΩ cm). The surface tension between the mica and the PS is greater than that between PS and water. This is to say that the equilibrium contact angle given by the Young-Dupré equation, Eq. 2.4, is larger for PS on mica than for water on mica. When the mica substrate containing the PS film is slowly dipped into water, the water wets between the mica and the PS, lifting the film from the substrate such that it floats atop the surface of the water. Since PS is hydrophobic (like a styrofoam cup), the film does not dissolve in the water and remains intact. Once the film is floating, we then take a Si substrate with a preexisting spincasted PS film also of ∼500 nm and pick up the floated film. By floating three films of ∼500 nm on top of each other we obtain the desired ∼2000 nm film.

To obtain PS microdroplets we use a dewetting technique. Dewetting is the process by which a film breaks into holes ultimately leading to small droplets as described in Section 2.1. First, we spincast a PS film of of thickness $e \sim 100$ nm on mica. The mica is then placed in a toluene saturated environment. The PS becomes liquid by absorbing toluene, and dewets due to the negative spreading coefficient. To ensure the dewetting process has gone to completion, the mica remains in the toluene rich environment for ∼24 h which results in spherical caps. All thin films on Si and droplets on mica are annealed in vacuum for at least 24 h at 150°C which is well above the glass transition of PS, $T_g \sim 100$°C. Annealing is important to ensure the polymer is in the equilibrium configuration and residual solvent has been removed.

It is also important for the films that were fabricated by floating to remove the interface between the floated films. When the droplets are removed from the toluene environment the fast evaporation of the toluene causes the droplets to become more flat on the top compared to a spherical cap. Annealing at a temperature above T_g ensures that the droplets are in fact spherical caps; we know surface tension dictates that the system geometry be such that the surface area to volume ratio is minimized. Annealing the droplets results in spherical caps with contact angle of $<15°$, radius $a \sim 10$ µm and height $d_0 \sim 1$ µm. An optical microscopy image of PS dewetted off mica is shown in Fig. 2.4. We have confirmed that this spherical cap assumption is valid with atomic force microscopy (AFM, Veeco Caliber).

Once we have sufficiently annealed both the droplets on mica and the thin films on Si we use a floating technique to obtain the desired sample configuration of a perfect spherical cap atop a thin film of PS. As described above, PS floats off mica. Thus, if we dip the mica substrate containing the droplets into water, the droplets float atop the surface. Although not visible by eye due to their small size, we can pick these droplets up using the thin PS film on Si. We are able to reliably fabricate the desired sample configuration using this spincasting, dewetting and floating procedure. Inherent in the dewetting process, a range of droplet sizes will be present. The film thickness, e, is also easily controlled as described above. Thus, we are able to control the aspect ratio, d_0/e, using this procedure.

Since the droplets are not visible by eye, we must view the sample on the optical microscope in reflection mode (Olympus, USA) to determine if we have successfully picked up the PS droplets. Using a red laser line filter ($\lambda = 632.8$ nm, Newport, USA) we look for characteristic Newton rings as can be seen in Fig. 3.2. Newton rings arise due to the interfering monochromatic light. Since PS is in the glassy state at room temperature we are able to carefully select the ideal droplet for the experiment before the droplet begins to level.

To observe the levelling behaviour of the PS droplets on the PS films we heat the system to 180°C on a microscope heating stage (Linkam, UK). This is well above the T_g of PS and the system becomes liquid and flows. The driving force for levelling is the gradient in Laplace pressure as described in Section 2.1. As the droplet spreads, Newton rings disappear and move radially outward. This is due to the height de-

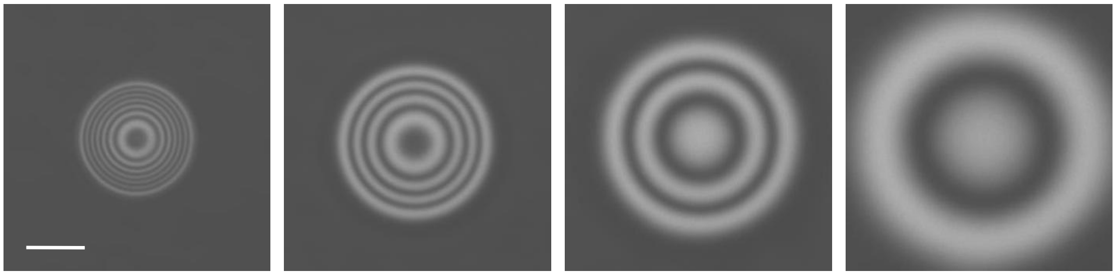

Figure 3.2:
Optical microscopy images of a PS droplet levelling on a film of thickness $e = 112$ nm. The first image is after 0 s of levelling, the second after ∼ 18 min, the third after ∼ 2 h and the fourth after ∼ 17 h. The scale bar is 10 µm. Alternating rings of bright and dark, known as Newton rings are visible due to the interference of light; the more rings present, the taller the droplet.

creasing and the radius increasing (see Fig. 3.2). The droplet levels fastest at the beginning and images are typically taken every 10 s. As the dynamics slow, pictures are taken every 10 min. A typical experiment can take anywhere from 1 h to 17 h depending on the initial aspect ratio of the system which results in 200 images to analyze the levelling behaviour. The analysis is described in Section 3.2.

3.1.2 Silicone Oil

Experiments were also performed using 100 000 cs silicone oil droplets (polydimetylsiloxane, Petrarch Systems Inc., USA). At room temperature, silicone oil is in the liquid state, thus, preparing well controlled samples is more difficult than with PS. As with PS, thin films of silicone oil were first spincast onto a Si wafer. To control the thickness we varied the spin speed as well as the concentration of silicone oil by dissolving the oil in toluene. Toluene is a good solvent for silicone oil. The thickness of the silicone oil films were measured using the scale on the optical microscope. By focusing first on the substrate, then on the surface and recording the amount the microscope stage moved during refocus, the film thickness can be determined. This method was used as the films were relatively thick (on the order of 10's of microns) and could not be measured with an ellipsometer or an AFM.

Droplets of silicone oil were deposited on the thin films using a thin wire. The spreading was observed using a contact angle measurement set-up; droplets were observed from the side rather than from the top as with the PS experiments. Spreading of silicone oil is much faster than PS due to the low viscocity. The typical size of the silicone oil droplets was on the order of 100's of microns in radius. This is an order of magnitude larger than the typical PS droplets studied. In addition, the timescale of levelling was anywhere from a few minutes to a few hours. Depending on the length of the experiment, images were taken with the optical microscope every 1 s to 10 s.

3.2 Analysis

Data analysis was performed using MATLAB. For each PS droplet experiment there were typically 200 images of the droplet spreading over the duration of the experiment. The first step in the analysis was to detect the centre of the droplet. Since the sample drifts as the system reaches equilibrium, the position of the centre of the drop is not constant. Different centre detection algorithms exists, however, it was found that as the droplet evolved in time, different parameters were needed to accurately detect the centre. In addition, if there were any defects on the sample or for samples with more than one droplet in the image, the centre detection algorithms would fail. The most reliable method was to click on the centre of the droplet for each image by eye. Once the centre had been obtained for each image, the radial average of each image was computed. This was done by scanning from the centre out in discrete increments. For a given distance from the centre, the intensity at that distance was averaged. A typical radial average is shown in Fig. 3.3.

As the droplet levels, the intensity of the centre changes periodically as each Newton ring disappears and the radius increases. This can be seen in the series of images for a single droplet experiment for various times of the experiment as seen in Fig. 3.2. By monitoring the change in intensity at the centre of the drop as a function of time we can determine the decrease in droplet height. The relationship between height and intensity is given by the thin film equations which are described in the Appendix, Chapter 7. To determine the absolute droplet height we subtract the underlying film height which can also be measured precisely using an imaging ellipsometer as described in Section 2.6.2.

The radius of the droplet is less well defined compared to the droplet height. It

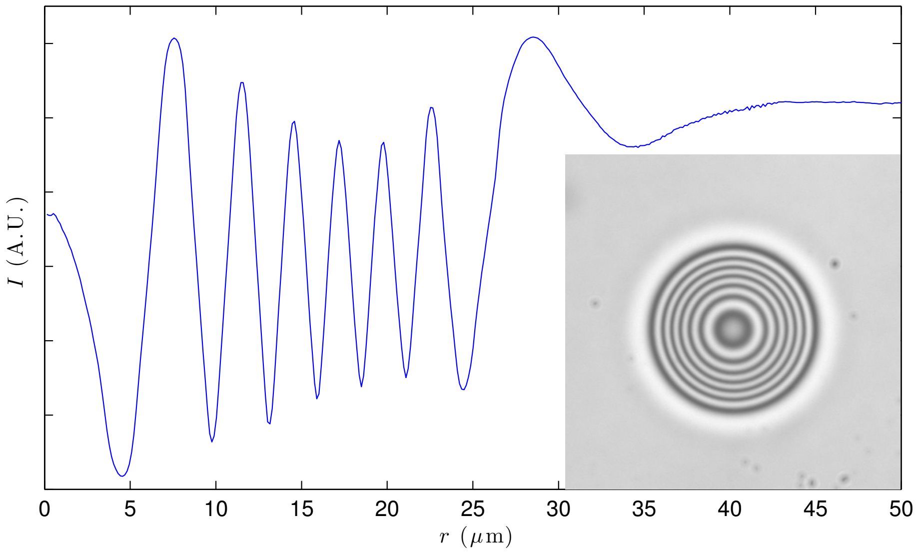

Figure 3.3:
Intensity, I, in arbitrary units as a function of radial position r in microns of a PS droplet on a thin PS film of 246 nm after heating for 800 s. This radial average was calculated from the optical image in the inset.

is difficult to determine where the droplet ends and the underlying film begins once the system is in the liquid state. Before heating the contact line is well defined and the radius can easily be determined. However, the high negative curvature at the contact line results in a dip as predicted by Tanner [21] and can be explained by the high negative Laplace pressure as discussed in Section 2.1 (see schematic in Fig. 3.4). This is clear in the radial average, (Fig. 3.3) where the intensity does not change drastically at the contact line indicating the radius is not well defined.

The volume of the droplet was determined through a few different methods. For some experiments an image before heating showed a well defined, perfect spherical cap with Newton rings clearly visible and periodic. For those experiments, a spherical cap approximation was used based on the well defined peak positions of the Newton rings (see Fig. 3.2). This is a perfect assumption before heating and gives an accurate value of the volume. It is important to note that upon heating, the system expanded and thus the volume measured at room temperature is reduced compared to the volume at 180°C, this was taken into account in the analysis. For some experiments a before heating image was not possible as there was occasionally air trapped between the

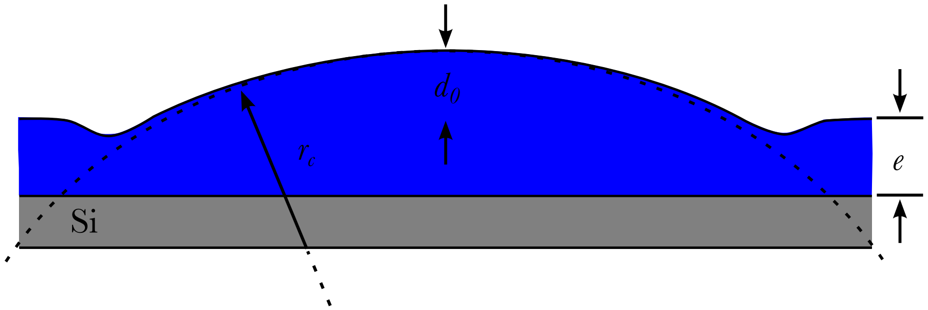

Figure 3.4:
Schematic of of a liquid droplet on a liquid film. The spherical cap fit is only valid at the top of the drop, near the edges the fit deviates due to the dip formed at the contact line. This dip formation is a result of high negative curvature before heating.

droplet and substrate film. When air is trapped, a non-uniform interference pattern that is not useful for determining the height results (see Fig. 3.5). As soon as such a droplet is heated above T_g the air disappears and well defined Newton rings are visible (see Fig. 3.5). For all experiments that did not contain a before heating image, the volume was determined from the first image after heating using a spherical cap fit to the peak positions. If the underlying film is thin in comparison to the droplet height, the spherical cap fit remains a strong assumption for the early images.

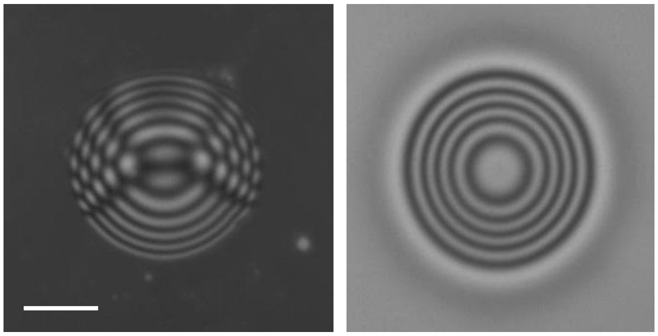

Figure 3.5:
Optical microscopy image of a droplet before heating (left) and directly after heating to 180°C (right). Before heating there is air trapped between the droplet and the film making it difficult to determine the droplet height. After heating the air is gone and the dip is formed around the circumference of the drop. Scale bar is 10 µm.

For droplets that were small in comparison to the underlying film thickness, the spherical cap fit was not a good assumption even for the very first image after heating. This is due to the high curvature at the contact line and the dip that forms as depicted schematically in Fig. 3.4. A more appropriate determination of the droplet volume was to use a Reimann sum using the peak positions of the Newton rings. The spherical cap approximation underestimated the volume while the Reimann sum overestimated the volume. Thus, we obtain an upper and a lower bound on the volume.

For each experiment the volume was determined through the methods described above and both the error, and estimated volume were determined. It will be apparent in Chapter 5 that the volume is needed to test for agreement between simulation and experiment using our theoretical model.

Chapter 4

Theoretical Model

To understand the underlying physical mechanism of this system we have developed a theoretical model along with our collaborators at the ESPCI in Paris, France, which is presented in it's entirety in the submitted manuscript in Chapter 5. In this Chapter a simple dimensional analysis based on the lubrication approximation will be presented that captures the scaling behaviour observed in experiment.

First, we assume a spherical cap geometry of the droplets. We know from AFM data that this assumption is valid at early times and as the droplet evolves in time becomes less valid due to the development of a dip at the contact line. This is shown schematically in Fig. 3.4. However, even at the late times the error associated with the spherical cap approximation is relatively small and as we will see this assumption leads to the proper scaling relation. We thus have,

$$a = \sqrt{2r_c d_0 - d_0^2} \sim \sqrt{2r_c d_0}, \tag{4.1}$$

where r_c is the radius of the spherical cap fit, d_0 is the height of the droplet and a is the radius of the cap (see Fig. 3.1). In Eq. 4.1 we have used the assumption that $d_0/r_c << 1$ which is valid in our experimental geometry as the contact angles are small.

The second assumption we make is that the volume of the cap is conserved. We know that the system volume, cap and film is conserved as polymers are non-volatile. In addition, we know that apart from the dip at the contact line, there is little perturbation in the film. Thus, volume assumption is valid and the expression for a spherical cap is given by,

$$V_{cap} = \frac{1}{6}\pi d_0(3a^2 + d_0^2) \sim \frac{1}{2}\pi d_0 a^2, \tag{4.2}$$

where again we have invoked the assumption that $d_0/r_c << 1$.

Lastly, we assume that the lubrication approximation is valid. The lubrication approximation is a good assumption because we are dealing with thin, viscous films with large lateral length scales in comparison to vertical length scales. In cylindrical coordinates with our droplet geometry the lubrication approximation takes the form,

$$\partial_t h + \frac{\gamma}{3\eta}\frac{1}{r}\partial_r \left[rh^3 \left(\partial_r^3 h + \frac{1}{r}\partial_r^2 h - \frac{1}{r^2}\partial_r h \right) \right] = 0, \tag{4.3}$$

where the height h is the height of the system, $h(r,t) = e + d(r,t)$ with e being the height of the substrate film and r is the radial distance from the centre of the drop [17, 18]. If we perform dimensional analysis on Eq. 4.3 using the dimensionless variables $H = h/H_0$ and $R = r/a$ we obtain,

$$a = \left(\frac{\gamma}{3\eta}\right)^{\frac{1}{4}} (H_0)^{\frac{3}{4}} t^{\frac{1}{4}}, \tag{4.4}$$

where H_0 is the total height of the system, $H_0 = d(r,t) + e$ and a is the radius depicted in Fig. 3.1.

If we combine Eq. 4.1, 4.2 and 4.3 we obtain the scaling relation,

$$\frac{r_c}{(H_0)^3} \sim \frac{\gamma}{V\eta} t. \tag{4.5}$$

Intuitively Eq. 4.5 makes sense, if the radius of the spherical cap fit is larger, the time it takes to spread must also be larger as the curvature of the system is less and the driving force is reduced. Similarly, if the total height H_0 is large, t is small due to Poiseuille flow. Thicker films have greater velocity at the air-liquid interface and can thus evolve at a faster rate.

If we perform a change of variables to Eq. 4.4 we obtain,

$$\left(\frac{d_0}{e}\right)^2 \left(1 + \frac{d_0}{e}\right)^3 = ct^{-1}, \tag{4.6}$$

where c is a constant that is described in full with the rigorous theoretical model presented in Chapter 5. Eq. 4.6 captures the relevant scaling of the problem and is written in terms of the experimentally controlled aspect ratio of droplet height to film height, d_0/e. In the one extreme regime, when the film height is small in comparison to the droplet height we recover Tanner's law, $d_0 \sim t^{-1/5}$. In the other extreme, when the film height is much larger than the droplet height we obtain a faster spreading law, $d_0 \sim t^{-1/2}$.

Chapter 5

Results

5.1 Preface

The experimental results of polymer droplets levelling on thin films of identical polymer are presented in the following paper that has been submitted to Physical Review Letters. I was the principle investigator which involved the sample preparation, conducting experiments, and analysis as described in Chapter 3. Every step of the way I was assisted by Joshua D. McGraw and Dr. Kari Dalnoki Veress. A theoretical model will be presented which accurately captures the physics of this system. This model was developed with our collaborators Dr. Thomas Salez and Dr. Elie Raphaël at the ESPCI in Paris, France.

Beyond Tanner's Law: Crossover Between Spreading Regimes of a Viscous Droplet on an Identical Film

Sara L. Cormier,[1] Joshua D. McGraw,[1] Thomas Salez,[2] Elie Raphaël,[2] and Kari Dalnoki-Veress[1,*]

[1] *Department of Physics & Astronomy and the Brockhouse Institute for Materials Research,*
McMaster University, Hamilton, ON, Canada
[2] *Laboratoire de Physico-Chimie Théorique, UMR CNRS Gulliver 7083, ESPCI, Paris, France*

(Dated: August 1, 2012)

We present results on the levelling of polymer micro-droplets on thin films prepared from the same material. In particular, we explore the crossover from a droplet spreading on an infinitesimally thin film (Tanner's law regime) to that of a droplet levelling on a film thicker than the droplet itself. In both regimes, the droplet's excess surface decreases towards the equilibrium configuration of a flat liquid film, but with a different power law in time. Additionally, the characteristic levelling time depends on molecular properties, the size of the droplet and the thickness of the underlying film. Flow within the film makes this system fundamentally different from a droplet spreading on a solid surface. We thus develop a theoretical model based on thin film hydrodynamics that quantitatively describes the observed crossover between the two levelling regimes.

If a liquid droplet is deposited onto a smooth solid surface with a relatively high surface energy, the droplet will spread. Several decades ago, it was shown that the height of the droplet decreases in time as $d_0 \sim t^{-1/5}$ if surface tension is the dominant driving force [1–10]. Interestingly, this so-called Tanner's law is valid for any simple liquid that wets a surface. The reason for this universality is that a precursor film emerges ahead of the bulk of the droplet [5, 10–17] which consumes the excess surface energy of the solid. The spreading of the droplets which follows the formation of the precursor film is driven by the excess surface of the non-flat liquid; in essence the droplet is spreading on a thin film of itself. However, as we show here, the power law changes if a droplet spreads on a thicker film that is already present. Specifically, a range of powers can be observed, depending on the precise thickness of the underlying film in comparison with the size of the droplet, with Tanner's law being a limiting case.

A simple example of a process in which the underlying precursor thickness changes is that of spraying liquid (*e.g.* paint) onto a wetting surface [18]. The first drops of sprayed paint spread according to Tanner's law [4], much like the sequence shown in Fig. 1(a). After the paint droplets have coalesced on the solid surface, a thin film of wet paint will have formed. Due to surface tension, new droplets that are deposited will spread on the thin paint film. The layer of paint deposited in the spray painting process will eventually become thicker than the precursor film (typically 0.1 nm to 10 nm thick [10]) in Tanner's law spreading. Thus, we must now consider that in addition to the flow within the liquid droplet, the film also contributes to the flow as the system evolves towards the lowest energy configuration of a flat surface; this is the situation depicted in Fig. 1(b). Comparison of the length and timescales in Fig 1 clearly demonstrates that for every subsequent layer of wet paint that is deposited, the characteristic levelling time of the droplet will change. This timescale will depend on the height of the underlying film as well as the size of the droplet.

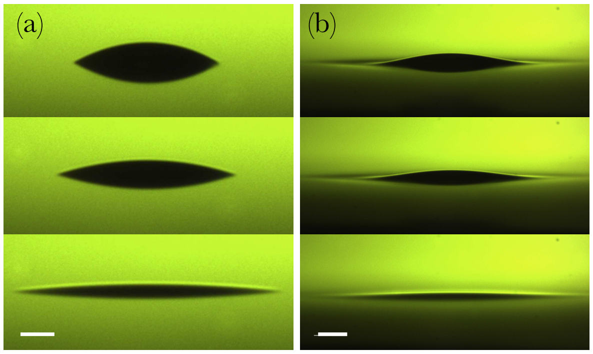

FIG. 1. Optical microscopy images of silicone oil droplets spreading on a thin film of the same oil. In the side view shown, the droplet and its reflection are clearly visible. (a) Droplet spreading on a film with thickness $e \sim 0.2$ µm. (b) Droplet spreading on a film with thickness $e \sim 22$ µm. The times between first and last images are ~ 45 min and ~ 1 min; and the scale bars are 100 µm and 250 µm respectively in (a) and (b).

It is difficult to fabricate well controlled samples of small liquid droplets atop identical thin liquid films; however, such systems have been studied computationally [14, 15, 19]. Molecular dynamics simulations have investigated polymer droplets spreading on glassy and liquid polymer substrates of varying molecular weights [19]. It was found that if the polymer droplet and the liquid polymer film are of a different molecular weight, the droplet simultaneously spreads and interpenetrates the polymer film. In addition, these molecular dynamics simulations clearly demonstrated a difference between droplets spreading on a glassy substrate and droplets spreading on a liquid substrate. In other studies, various spreading laws were found for liquid droplets spreading on an imiscible liquid, dependending on the relative

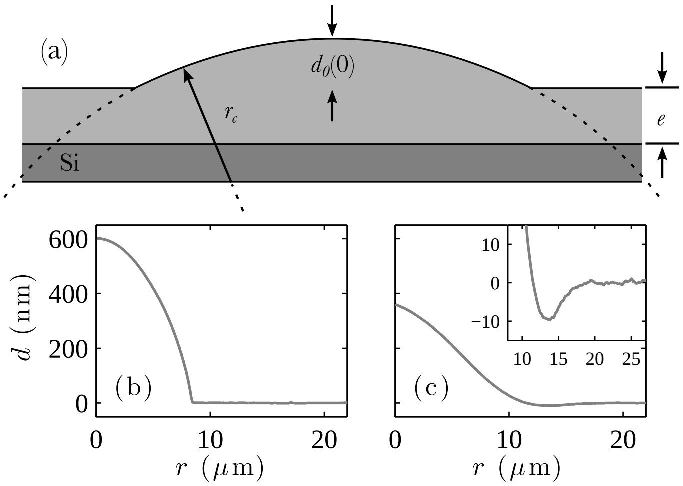

FIG. 2. (a) Initial geometry: a spherical cap with radius of curvature r_c and height $d_0(0)$ atop a thin film of identical material with height e supported on a Si substrate. (b) AFM line profile $d(r, 0)$ of a PS droplet on a thin PS film ($e =$ 201 nm) before heating ($t = 0$) as a function of the distance r to the center of the droplet. (c) AFM profile $d(r, t)$ for the same droplet after heating at 180°C for $t = 20$ min. The inset shows the same data as in (c) with d and r ranges chosen to emphasize the dip in the film surface at the periphery of the droplet.

viscosities [20–23]. Here, we will see that the spreading law can vary even for a droplet spreading on an identical film, the key parameter being the aspect ratio between the drop height and the film height d_0/e.

It is the difference between spreading on a thick versus a thin film that is the focus of this Letter. We develop an understanding of the crossover from Tanner's law spreading to the case of a droplet levelling on a film of the same liquid that is relatively thick. Specifically, we investigate how the dynamics of droplet spreading depends on the aspect ratio. The physics is both general and ubiquitous, from the spreading of a droplet of rain on a wet road, to the levelling of a droplet of paint.

The images in Fig. 1 show the levelling of 100 000 cs silicone oil droplets (polydimetylsiloxane, Petrarch Systems Inc., USA) with initial radius of curvature $r_c \sim 1$ mm. Underlying films were made by spin casting the oil directly onto Si substrates. Droplets of the same oil were deposited onto the film and images were obtained using a simple contact angle measurement set-up. Since the silicone oil is liquid at room temperature, it is difficult to control precisely the initial height profile of droplets on films prepared in this way.

An ideal initial sample geometry is that of a spherical cap atop a thin film of an identical liquid shown schematically in Fig. 2(a). Samples with such a geometry were prepared using another material: polystyrene (PS), which has a glass transition $T_g \sim 100$°C. The weight averaged molecular weight of the PS was $M_w = 118$ kg/mol with a polydispersity index of 1.05 (Polymer Source Inc., Canada). PS dissolved in toluene was spin cast onto thin sheets of freshly cleaved mica (Ted Pella Inc., USA). The resulting films were ~ 100 nm thick. Thin films of the same PS in toluene with various concentrations were spin cast onto 10×10 mm^2 Si substrates. The films on the Si substrates ranged in thickness from $e \sim 50$ nm to 2000 nm as measured by ellipsometry (EP3, Accurion, Germany). The PS films on mica were placed in a saturated toluene atmosphere. The PS, which is well below the glass transition at room temperature, absorbs toluene, becomes liquid, and readily dewets from the mica substrates. The resulting droplets ranged in size, with typical $r_c \sim 100$ µm and height $d_0(0) \sim 1$ µm. Both the droplets on mica and the thin films on Si were annealed in vacuum (10^{-5} mbar) for 24 h at 150°C, which is well above T_g. The annealing is much longer than the longest relaxation time for the polymer used, removes residual solvent, and forms PS spherical caps on the mica substrate with contact angle less than 15° as measured with atomic force microscopy (AFM, Veeco Caliber), see Fig. 2(b).

At room temperature, with PS in the glassy state, the entire mica sheet was dipped into clean water (Milli Q, 18.2 MΩ cm) and droplets floated atop the surface due to the hydrophobicity of PS. The film of PS on Si was skimmed across the surface of water containing the floating droplets. Droplets were thus picked up by the PS film resulting in the desired sample configuration as shown in Fig. 2(a). With this sample preparation, we were able to easily control the initial aspect ratio of the system, which had a range of $0.1 \leq d_0(0)/e \leq 100$. Though we focus here on the simplest symmetric system for the droplet and film, polymers of different M_w, or different chemical composition can also be prepared.

To observe droplet levelling, the samples were rapidly heated to 180°C, well above T_g, on a heating stage (Linkam, UK). All experiments with PS were performed using optical microscopy in reflection (Olympus, USA) and illuminated with a red laser line filter ($\lambda = 632.8$ nm, Newport, USA). Images were obtained for 1 h to 17 h, depending on the initial aspect ratio. Once PS is in the melt state, the Laplace pressure acts to reduce the curvature gradients and the droplet levels (see video in the supplementary material [24].

Initially, at the contact line where the spherical cap meets the PS film, there is a high negative radial curvature. This curvature is sharpest prior to heating, as can been seen in the AFM line profile shown in Fig. 2(b), where the droplet profile $d(r, 0)$ is shown as a function of the radial position r from the centre of the droplet. The pressure gradients result in a dip around the circumference of the drop (Fig. 1(b) and Fig. 2(c)); similar features appear in the relaxation of stepped surface profiles [25] and were predicted in droplets on films by Tanner [4]. At early times, the curvature gradients are strongest near the dip, and this region dominates the flow. At later times, the curvature at the top of the droplet dominates and the entire droplet levels. It is the later time regime that is the focus of this Letter.

Fig. 1 and Fig. 2 illustrate the role of the underlying film. A droplet with a large height d_0 in comparison to the film thickness e, spreads much like Tanner's wetting droplet (see Fig. 1(a)). In this case the infinitesimal film is like a precursor film. In contrast, a droplet on a film that is thicker spreads in a way that is qualitatively different. From Fig. 1(b) and Fig. 2(c) it is clear that the liquid surface of the film is perturbed well beyond the position of the initial contact line. Furthermore, the characteristic levelling times in Fig. 1 are vastly different: though in the first frames shown the droplet heights differ by only a factor of ~ 3, the timescales in the sequence vary by a factor of ~ 50.

We now turn to a full description of the experiments using PS droplets on PS films, we show in Figs. 3(a) and 3(b) optical microscopy images of a droplet before and after 15 h of annealing. Newton rings are observed as a result of interfering monochromatic light reflecting from both the air-PS and PS-Si interfaces. The intensity $I(r,t)$ changes periodically with total height $h(r,t)$ with respect to the substrate, as described by the optical thin film equations [26]. We monitor the change in the intensity at the centre of the drop with time, as seen in Fig. 3(c), and determine the central height $h(0,t)$ [27]. Fig. 3(d) shows $d_0(t) = d(0,t) = h(0,t) - e$ for two independent droplet levelling experiments with different aspect ratios, d_0/e. Comparing the two experiments, we observe that the long time data can be described by two different power laws. If the droplet height is large in comparison to the film (triangles), we observe a spreading law that approaches Tanner's law: $d_0 \sim t^{-n}$, with $n = 0.22 \approx 1/5$. In the limit $d_0/e \to \infty$, the thin film is thus identical to the precursor film of a Tanner's law droplet. On the other hand, when d_0/e is small (squares), we observe spreading with a stronger time dependence than Tanner's law, characterized by $d_0 \sim t^{-n}$ with $n = 0.38 > 1/5$. The system evolves faster when the film height is larger.

In the following, we derive a theoretical model in order to unify the experimental results in all regimes. Firstly, since the height scale is small compared to typical radial scales, the lubrication approximation [6, 28, 29] can be used. Secondly, the droplet levelling is driven by gradients in the Laplace pressure. This pressure is proportional to both the surface tension, γ, at the air-fluid interface, and the two principal curvatures. The height scales involved in these experiments allow us to neglect the hydrostatic [6, 30] and disjoining pressures [31, 32]. Thirdly, since we consider a highly viscous fluid with viscosity, η, it is reasonable to use the Stokes' equation to connect the local velocity and pressure. Finally, we assume incompressibility of the flow. Therefore, according to the cylindrical geometry of the system studied, the capillary driven thin film equation

$$\partial_t h + \frac{\gamma}{3\eta}\frac{1}{r}\partial_r \left[r h^3 \left(\partial_r^3 h + \frac{1}{r}\partial_r^2 h - \frac{1}{r^2}\partial_r h \right) \right] = 0 \ , \qquad (1)$$

describes the evolution of the total height of the free interface: $h(r,t) = e + d(r,t)$. In addition, we assume that the underlying film of constant thickness e is infinite in lateral extent. Compared to the analysis of [33, 34], the geometry of our system requires us to retain the last two terms in Eq. (1).

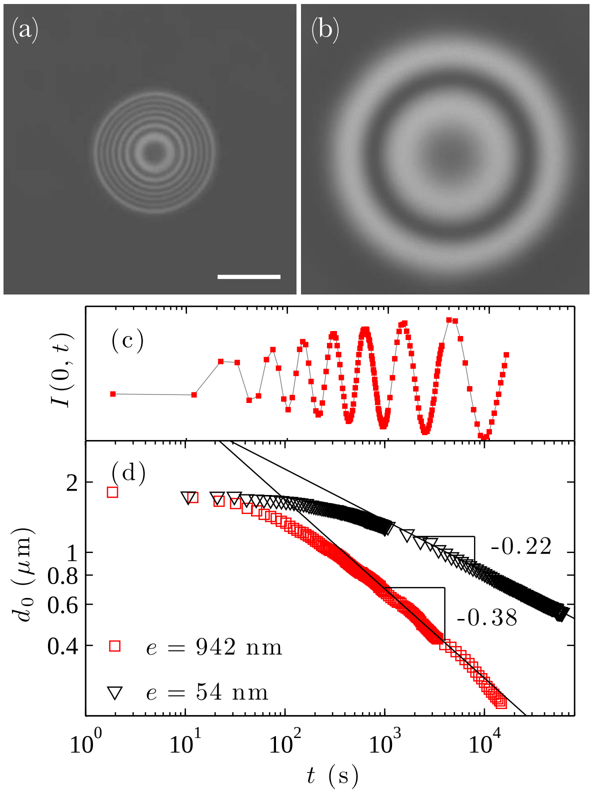

FIG. 3. Optical microscopy images showing the Newton rings of the droplets on a thin film (a) before and (b) after heating for 15 h (10 µm scale bar). (c) Intensity at the centre of the droplet as a function of time. (d) Temporal power-law decrease in droplet height for two independent droplet experiments. In (c) and (d) the squares correspond to the droplet shown in (a) and (b).

We non-dimensionalize the problem through: $D = d/e$, $D_0 = d_0/e$, $R = r/e$, $R_c = r_c/e$ and $T = \gamma t/(3\eta e)$, and we assume the existence of self-similar solutions of the form

$$D(R,T) = D_0(T) F(U) \ , \qquad (2)$$

where

$$U = \frac{R}{T^{1/4}\left[1 + D_0(T)\right]^{3/4}} \ . \qquad (3)$$

This particular horizontal scaling is analogous to the one proposed in [34], except that we take into account the time dependence of the typical height through $D_0(T)$. Note that this scaling is not valid at early times for the reason given above: the short time dynamics is governed by the radial curvature at the edge of the droplet. In the following, we assume that such a self-similar solution is reached after a certain time depending on the initial geometry. The self similarity has been experimentally verified using AFM profiles such as the one in Fig. 2(c).

The additional volume V with respect to the volume of the underlying film is constant by incompressibility, and equals $V = 2\pi e^3 \int_0^\infty dR\ R\ D(R,T)$. Using Eq. (2) and Eq. (3) we get the time evolution of the droplet height

$$\left(\frac{d_0}{e}\right)^2 \left(1 + \frac{d_0}{e}\right)^3 = \frac{\tau}{t} \ . \tag{4}$$

The characteristic levelling time, τ, is given by

$$\tau = \frac{1}{\alpha^2}\ \frac{\eta V^2}{\gamma e^5} \ , \tag{5}$$

where

$$\alpha = \frac{2\pi}{\sqrt{3}} \int_0^\infty dU\ U\ F(U), \tag{6}$$

is a geometrical factor depending only on the dimensionless height $D_0(0)$ and radius of curvature R_c of the initial spherical droplet. If we examine the limits of Eq. (4), we find that for $d_0 \gg e$ Tanner's law is recovered: $d_0 \sim t^{-1/5}$. In contrast, for $d_0 \ll e$ we get $d_0 \sim t^{-1/2}$: the model predicts that a droplet of a given size will level faster on a thicker film, in accordance with the simple observations made for the silicone oil droplet sequences in Fig. 1 and the PS data in Fig. 3(d).

To test the model prediction of Eq. (4), we performed 35 independent droplet levelling experiments of the type shown in Fig. 3 using PS. For each experiment the initial aspect ratio $d_0(0)/e$ and volume V were different. The evolution of d_0 was then compared to Eq. (4). For each sample, we determine V using the optical microscopy images, and e as described above. In addition, we measure $\gamma/\eta = 3.2$ µm/s using the stepped bilayer analysis of [35]. Therefore, α in Eq. (6) is the only adjustable parameter in a fit to Eq. (4) and Eq. (5). We find experimentally that $4 < \alpha < 15$ for the studied samples and that α varies monotonically with the aspect ratio. Using the experimentally determined aspect ratio and radius of curvature, we also calculate α from numerical solutions to the nonlinear partial differential Eq. (1) [37]. Experimentally and numerically determined values agree and both the spread and trend observed are consistent with the theory. The results of all PS droplet levelling experiments in this study are plotted in Fig. 4 where it can be seen that the data accesses 12 orders of magnitude in scaled time. Moreover, the result clearly shows that the droplet levelling dynamics depends sensitively on the aspect ratio of the system through the flow in the underlying film.

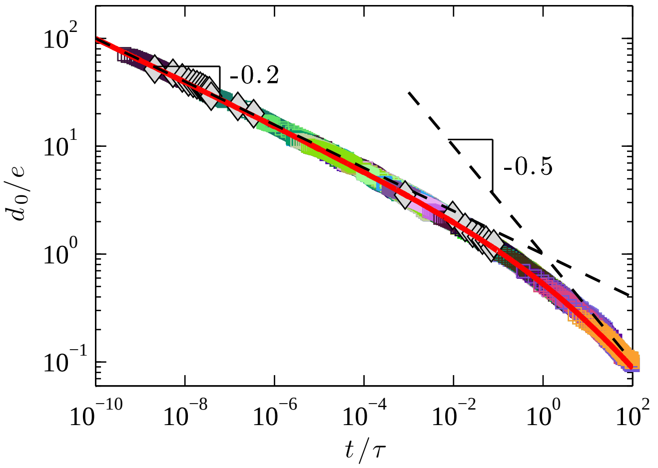

FIG. 4. Plot of the droplet-film aspect ratio as a function of the renormalized time defined by Eq. (5). The plot contains 35 experiments with PS droplets (squares, various colours) as well as the curve corresponding to the model of Eq. (4) (red solid line). The Tanner limit ($d_0 \gg e$) and thick film limit ($d \ll e$) are shown with dashed lines. Grey diamonds correspond to the data for the silicone oil droplet experiment from Fig. 1.

Since the previous model assumes only that the levelling is driven by the Laplace pressure and that the thin film equation applies, the result has to be general and should hold for any thin and non-volatile viscous fluid. To test this statement, the preliminary silicone oil data from Fig. 1 was added to the master plot in Fig. 4 (diamonds). In comparison to the experiments with PS droplets, the oil is two orders of magnitude less viscous and the characteristic length scales two orders of magnitude larger; nevertheless, both the silicone oil and PS data collapse, consistent with the theoretical prediction.

In this Letter, we have presented our work on the levelling of a viscous droplet on a film of the same liquid. It was found that the spreading law is controlled by the aspect ratio of the droplet height to the film height. To describe this spreading dependency, we developed a model based on a Laplace pressure driven viscous flow. The model predicts a crossover in the power law of spreading from the $d_0 \gg e$ Tanner regime, with $d_0 \sim t^{-1/5}$, to the case of $d_0 \ll e$ for a droplet levelling on a thicker film, with $d_0 \sim t^{-1/2}$. The model has been verified by experiments carried out using PS and silicone oil droplets, with initial aspect ratios ranging from $d_0(0)/e \sim 0.1$ to 100. The crossover from Tanner's law spreading to droplets levelling on films is a general result that holds for any non-volatile fluid in the thin film geometry.

The authors thank NSERC of Canada, the École Normale Supérieure of Paris, and the Saint-Gobain fellowship for financial support.

---

[*] dalnoki@mcmaster.ca

[1] C. Huh and L. E. Scriven, Journal of Colloid and Interface Science, **35**, 85 (1971).
[2] R. Hoffman, Journal of Colloid and Interface Science, **50**, 228 (1975).
[3] O. Voinov, Fluid Dynamics, **11**, 714 (1976).
[4] L. H. Tanner, Physics, **12** (1979).
[5] P. G. de Gennes, Rev. Mod. Phys., **57** (1985).
[6] P. G. de Gennes, F. Brochard-Wyart, and D. Quéré, *Capillarity and Wetting Phenomena: Drops, Bubbles, Pearls, Waves* (Springer, 2003).
[7] T. Blake, Journal of Colloid and Interface Science, **299**, 1 (2006).
[8] A. B. Croll and K. Dalnoki-Veress, The European Physical Journal E, **29**, 239 (2009).
[9] L. Courbin, J. C. Bird, M. Reyssat, and H. A. Stone, Journal of Physics: Condensed Matter, **21**, 464127 (2009).
[10] D. Bonn, J. Eggers, J. Indekeu, J. Meunier, and E. Rolley, Rev. Mod. Phys., **81**, 739 (2009).
[11] D. Ausserré, A. M. Picard, and L. Léger, Phys. Rev. Lett., **57**, 2671 (1986).
[12] M. P. Brenner and A. Bertozzi, Phys. Rev. Lett., **71**, 593 (1993).
[13] A. M. Cazabat, S. Gerdes, M. Valignat, and S. Villette, Interface Science, **5**, 129 (1997).
[14] D. R. Heine, G. S. Grest, and E. B. Webb, Physical Review E, **68**, 061603 (2003).
[15] A. Milchev and K. Binder, Journal of Chemical Physics, **116**, 7691 (2002).
[16] H. P. Kavehpour, B. Ovryn, and G. H. McKinley, Phys. Rev. Lett., **91**, 1996104 (2003).
[17] A. Hoang and H. P. Kavehpour, Phys. Rev. Lett., **106**, 254501 (2011).
[18] S. Jung and I. Hutchings, Soft Matter, **8**, 2686 (2012).
[19] F. Pierce, D. Perahia, and G. S. Grest, Europhysics Letters, **86**, 64004 (2009).
[20] J. Fraaije and A. M. Cazabat, Journal of Colloid and Interface Science, **133**, 452 (1989).
[21] L. Bacri and G. Debregeas, Langmuir, **1**, 6708 (1996).
[22] F. Brochard-Wyart, G. Debregeas, and P. G. de Gennes, Colloid & Polymer Science, **274**, 70 (1996).
[23] P. G. de Gennes, Polymer, **72**, 70 (1996).
[24] See Supplementary Material at **URL** for a typical PS droplet levelling experiment.
[25] J. D. McGraw, N. M. Jago, and K. Dalnoki-Veress, Soft Matter, **7**, 7832 (2011).
[26] O. Heavens, Rep. Prog. Phys., **23** (1960).
[27] To determine the height of the droplets we use the optical thin film equations in [26] along with the indices of refraction of Si, PS and air at 180°C, respectively: $n_{Si} = 3.9, n_{PS} = 1.53$ and $n_{air} = 1$. See [25] for details.
[28] A. Oron, S. H. Davis, and S. G. Bankoff, Rev. Mod. Phys., **69**, 931 (1997).
[29] R. V. Craster and O. K. Matar, Rev. Mod. Phys., **81**, 1131 (2009).
[30] F. Brochard-Wyart, H. Hervet, C. Redon, and F. Rondelez, Journal of Colloid and Interface Science, **142**, 518 (1991).
[31] E. Pérez, E. Schäffer, and U. Steiner, Journal of Colloid and Interface Science, **234**, 178 (2001).
[32] M. Ghosh and K. Stebe, Advances in Colloid and Interface Science, **161**, 61 (2010).
[33] L. E. Stillwagon and R. G. Larson, Physics of Fluids A: Fluid Dynamics, **2**, 1937 (1990).
[34] L. E. Stillwagon and R. G. Larson, J. of App. Phys., **63**, 5251 (1988).
[35] J. D. McGraw, T. Salez, O. Bäumchen, E. Raphaël, and K. Dalnoki-Veress, *Self-similarity and energy dissipation in stepped bilayer thin polymer films*, submitted. (2012).
[36] A. Bertozzi, Notices Amer. Math. Soc., **45** (1998).
[37] T. Salez, J. D. McGraw, S. L. Cormier, O. Bäumchen, K. Dalnoki-Veress, and E. Raphaël, *Numerical solutions of thin film equations for polymer flows*, to be published elsewhere. (2012).

5.2 Extended Results

In this section the results that were presented in the paper of the previous section will be expanded upon. Specifically, the relationship between the coefficient α in the theoretical model presented in the paper and the initial aspect ratio, $d_0(0)/e$ will be discussed. The time to reach self-similarity, t_o will also be investigated. For the 35 PS droplet experiments that were presented in the paper, the value of α was calculated and the errors computed and plotted as a function of $\log(d_0(0)/e)$ which is displayed in Fig. 5.1. While the data is noisy and the error bars large, it is clear that as the aspect ratio of the system increases, the value of alpha decreases. This decrease appears to be exponential. The range of α values determined experimentally agree well with the values determined through simulations, these simulations values are also plotted in Fig. 5.1. A future publication that is currently in preparation will describe in detail the numerical simulations used in computing the α values [64].

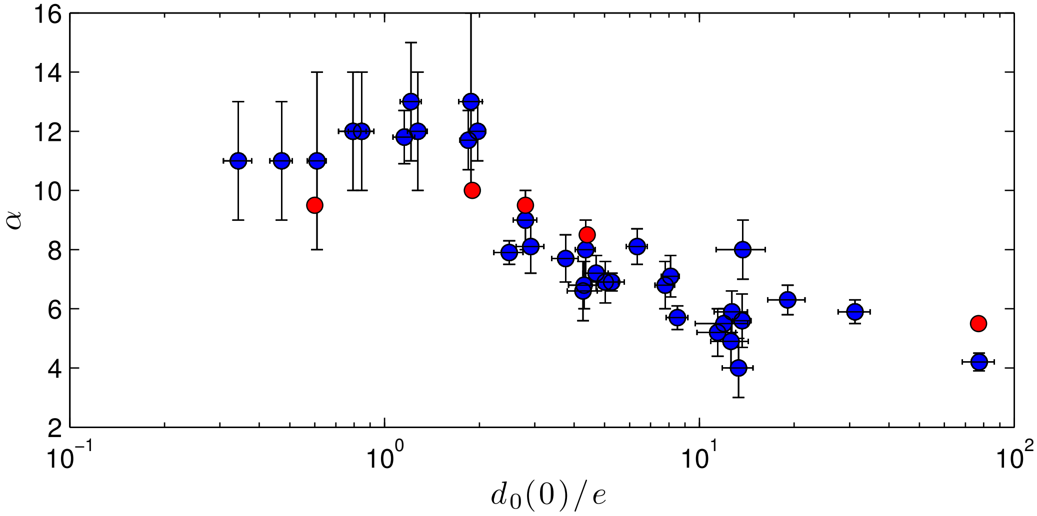

Figure 5.1:
The blue data is the experimentally determined α as a function of initial aspect ratio of the system. The red data is from simulations carried out by our collaborators Thomas Salez and Elie Raphaël at the ESPCI in Paris, France.

While it is technically incorrect to describe a droplet spreading on a liquid film with a power law, for the duration of an individual experiment it is valid once self-similarity has been reached. Self-Similarity is achieved faster when the aspect ratio is smaller (thicker film compared to drop height). This makes sense as the ability for the underlying film to flow is greater in the thicker film. At early times, the curvature at the contact line is sharpest and the driving force for flow is dominated in this region. It is during these early times that the dip forms. The drop does not level with a characteristic power-law behaviour until the dip has formed, and the sharp curvature at the contact line has been reduced. The theoretical model that we have developed deals with the dynamics of droplet levelling, thus, the model only applies to the data after some time t_o has passed. We have experimentally determined this time, t_o by observing when the droplet height as a function of aspect ratio behaves as a power-low. This experimentally determined t_o is plotted as function of $\log(d_0(0)/e)$ as shown in Fig. 5.2. The relationship is not very clear, however the general trend is as predicted. A larger aspect ratio corresponds to the greatest time to observe power-law spreading. In the small aspect ratio case, the t_o is small and the spreading is dominated by the bulk droplet curvature.

The large noise in Fig. 5.2 can in part be attributed to experimental conditions. There is always some error associated to assigning the $t = 0$ time of the experiment. The microscope and stage take time to reach thermal equilibrium and it takes time to focus the microscope before beginning the experiment. In addition, while we tried to ensure droplets were in equilibrium before beginning the experiment, it is possible that this was not always the case. It is also possible that this time to reach self-similarity depends on more than just the initial aspect ratio and may have a volume dependence.

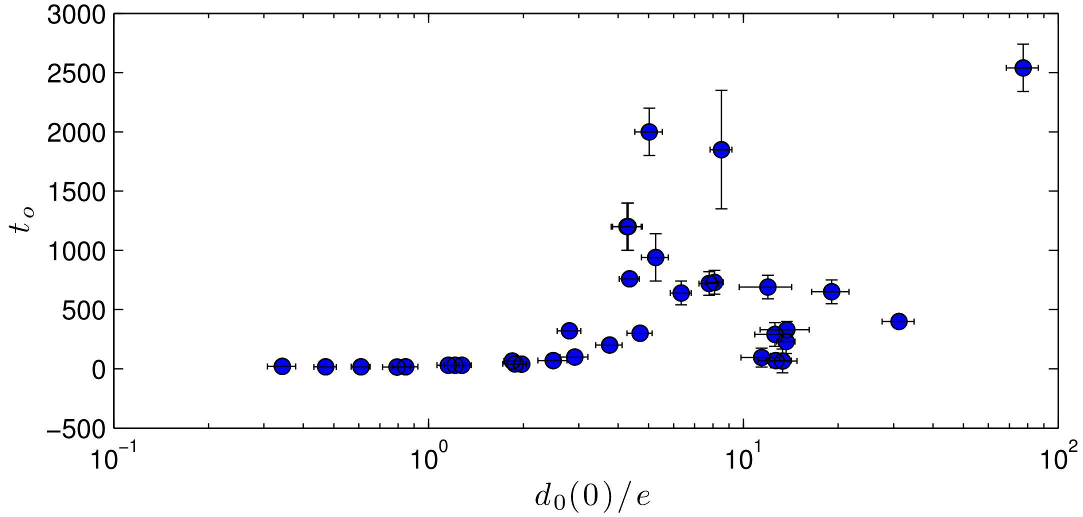

Figure 5.2:
Time to reach self-similarity t_0 as a function of the initial system aspect ratio.

Chapter 6

Conclusions

The spreading and levelling behaviour of liquids is an intense research area and has applications in wide ranging fields such as liquid coatings, spray painting and inkjet printing. It is not only important to understand the spreading behaviour of liquids on solids but also how liquids level on films of identical liquid. However, experimentally, a system of liquid spherical caps on liquid films can be difficult to study in a controllable manner as fabricating perfect spherical caps atop thin liquid films can be challenging.

In this thesis we have presented results of PS drops levelling on thin films of PS. Samples were fabricated at room temperature, with PS in the glassy state, using a method of spincasting, dewetting and floating. This preparation method allowed for precise control over the aspect ratio of the system. By heating above T_g, the levelling behaviour was observed for systems with varying aspect ratios.

We observed a crossover between droplets spreading on thin films, Tanner's law spreading, $d_0 \sim t^{-1/5}$ to that of small drops levelling on thicker films, $d_0 \sim t^{-1/2}$. This crossover has been captured with our theoretical model which is based on the lubrication approximation for thin films and is dependent on the system aspect ratio, d_0/e.

Experiments were also performed using a system of silicone oil. At room temperature silicone oil is in the liquid state, thus controllability of sample geometry was more difficult. Nonetheless, all the data fell on the theoretical model curve when rescaled. The silicone oil system was two orders of magnitude larger than that of the PS and yet the theoretical model remains valid. This shows the universality of the model being restricted only to non-volatile fluids in the thin film regime. By rescaling the PS and silicone oil data according to the theoretical model we are able to access twelve orders of magnitude in rescaled time.

Chapter 7

appendix

7.1 Optical Thin Film Equations

In order to determine the decrease in droplet height using the intensity data we have used the thin film equations. We have assumed that the intensity of light in the film varies only with the vertical height of the film [65]. The reflectance of light is given by,

$$R(h) = \frac{A - B + C\cos(2kh)}{A + B + C\cos(2kh)}, \tag{7.1}$$

where R is the reflectance, h the height, A, B, C, and k are constants defined below [66].

The constants in Eq. 7.1 are defined by,

$$A = (n_a^2 + n_p^2)(n_p^2 + n_s^2), \tag{7.2}$$

$$B = 3n_a n_p^2 n_s, \tag{7.3}$$

$$C = (n_a^2 - n_p^2)(n_p^2 - n_s^2), \tag{7.4}$$

$$k = 2\pi n_p/\lambda, \tag{7.5}$$

where $n_s = 3.9$ is the index of refraction of the silicon substrate, $n_a = 1$ is the index of refraction of air, $n_p = 1.53$ is the index of refraction of PS at 180°C and $\lambda = 633$ nm is the wavelength of light incident on the sample. Since all the constants in Eq. 7.1 are known, the reflectance as a function of film height can be determined. The first minimum of R occurs at 103.2 nm and the first maximum at 206.4 nm. The function is periodic and maximum/minimum occur every 103.2 nm. This information allows us to precisely determine the height profile of the PS droplets using the radial average.

Bibliography

[1] E. B. Dussan. On the spreading of liquids on solid surfaces: static and dynamic contact lines. *Ann. Rev. Fluid Mech.*, 11:371, 1979.

[2] P-.G. de Gennes. Wetting: statics and dynamics. *Rev. Mod. Phys.*, 57, 1985.

[3] L. Leger and J. F. Joanny. Liquid spreading. *Rep. Prog. Phys.*, 55:431, 1992.

[4] A. M. Cazabat, S. Gerdes, M. P. Valignat, and S. Villette. Dynamics of wetting: from theory to experiment. *Interface Science*, 5:129, 1997.

[5] D. Bonn and D. Ross. Wetting transitions. *Rep. Prog. Phys.*, 64:1085, 2001.

[6] P.-G. de Gennes, F. Brochard-Wyart, and D. Quéré. *Capillarity and Wetting Phenomena: Drops, Bubbles, Pearls, Waves.* Springer, 2003.

[7] T. D. Blake. The physics of moving wetting lines. *Journal of Colloid and Interface Science*, 299:1, 2006.

[8] D. Bonn, J. Eggers, J. Indekeu, J. Meunier, and E. Rolley. Wetting and spreading. *Rev. Mod. Phys.*, 81:739, 2009.

[9] L. Courbin, J. C. Bird, M. Reyssat, and H. A. Stone. Dynamics of wetting: from inertial spreading to viscous imbibition. *Journal of Physics: Condensed Matter*, 21:464127, 2009.

[10] F. Brochard-Wyart, H. Hervet, C. Redon, and F. Rondelez. Spreading of heavy drolets i. theory. *Journal of Colloid and Interface Science*, 142:518, 1991.

[11] T. Young. An essay on the cohesion of fluids. *Philos. Trans. R. Soc. London*, 95:65, 1805.

[12] C. Redon, F. Brochard-Wyart, and F. Rondelez. Dynamics of dewetting. *Phys. Rev. Lett.*, 66:715, 1991.

[13] G. Reiter. Dewetting of thin polymer films. *Phys. Rev. Lett.*, 68:75, 1992.

[14] R. Xie, A. Karim, J. F. Douglas, C. C. Han, and R. A. Weiss. Spinodal dewetting of thin polymer films. *Phys. Rev. Lett.*, 81:1251, 1998.

[15] R. Seeman, S. Herminghaus, and K. Jacobs. Dewetting patterns and molecular forces: A reconciliation. *Phys. Rev. Lett.*, 86:5534, 2001.

[16] D. Rind. Complexity and climate. *Science*, 284:105, 1999.

[17] L. E. Stillwagon and R. G. Larson. Fundamentals of topographic substrate leveling. *J. of App. Phys.*, 63:5251, 1988.

[18] L. E. Stillwagon and R. G. Larson. Leveling of thin films over uneven substrates during spin coating. *Physics of Fluids A: Fluid Dynamics*, 2:1937, 1990.

[19] J. Becker and Grün G. The thin-film equation: recent advances and some new perspectives. *Journal of Physics: Condensed Matter*, 17:S291, 2005.

[20] A. Oron, S. H. Davis, and S. G. Bankoff. Long-scale evolution of thin liquid films. *Rev. Mod. Phys.*, 69:931, 1997.

[21] L. H. Tanner. The spreading of silicone oil drops on horizontal surfaces. *Physics*, 12:1473, 1979.

[22] O. V. Voinov. Hydrodynamics of wetting (english translation). *Fluid Dynamics*, 11:714, 1976.

[23] R. L. Hoffman. Study of the advancing interface. *Journal of Colloid and Interface Science*, 50:228, 1975.

[24] J.-D. Chen. Experiments on a spreading drop and its contact angle on a solid. *Journal of Colloid and Interface Science*, 122:60, 1988.

[25] J.-D. Chen and N. Wada. Wetting dynamics of the edge of a spreading drop. *Phys. Rev. Lett.*, 62:3050, 1989.

[26] M. P. Brenner and A. Bertozzi. Spreading of Droplets on a Solid Surface. *Phys. Rev. Lett.*, 71:593, 1993.

[27] M. Fermigier and Jenffer P. An experimental investigation of the dynamic contact angle in liquid-liquid systems. *Journal of Colloid and Interface Science*, 146:226, 1991.

[28] P. Raiskinmäki, A. Koponen, J. Merikoski, and J. Timonen. Spreading dynamics of three-dimensional droplets by the lattice-boltzmann method. *Computational Materials Science*, 18:7, 2000.

[29] A. Milchev and K. Binder. Droplet spreading: a monte carlo test of tanner's law. *Journal of Chemical Physics*, 116:7691, 2002.

[30] L. Leger, M. Erman, A .M. Guinet-Picard, D. Ausserre, and C. Strazielle. Precursor film profiles of spreading liquid drops. *Phys. Rev. Lett.*, 60:2390, 1988.

[31] H. P. Kavehpour, B. Ovryn, and G. H. McKinley. Microscopic and macroscopic strucure of the precursor layer in spreading viscous drops. *Phys. Rev. Lett.*, 91:1996104, 2003.

[32] W. B. Hardy. The spreading of fluids on glass. *Philos. Mag.*, 38:49, 1919.

[33] P. Silberzan and L. Léger. Spreading of high molecular weight polymer melts on high-energy surfaces. *Macromolecules*, 25:1267, 1992.

[34] E. Pérez, E. Schäffer, and U. Steiner. Spreading Dynamics of Polydimethylsiloxane Drops: Crossover from Laplace to Van der Waals Spreading. *Journal of Colloid and Interface Science*, 234:178, 2001.

[35] A. B. Croll and K. Dalnoki-Veress. Spreading of diblock copolymer droplets: a probe of polymer micro-rheology. *The European Physical Journal E*, 29:239, 2009.

[36] A. Hoang and H. P. Kavehpour. Dynamics of Nanoscale Precursor Film near a Moving Contact Line of Spreading Drops. *Phys. Rev. Lett.*, 106:254501, 2011.

[37] G. He and N. G. Hadjiconstantinou. A molecular view of tanner's law: molecular dynamics simulations of drolet spreading. *J. Fluid Mech.*, 497:123, 2003.

[38] D. R. Heine, G. S. Grest, and E. B. Web III. Spreading dynamics of polymer nanodroplets. *Physical Review E*, 68:061603, 2003.

[39] D. R. Heine, G. S. Grest, and E. B. Webb. Surface wetting of liquid nanodroplets: Droplet-size effects. *Phys. Rev. Lett.*, 95:107801, 2005.

[40] D. Ausserré, A. M. Picard, and L. Léger. Existence and Role of the Precursor Film in the Spreading of Polymer Liquids. *Phys. Rev. Lett.*, 57(21):2671, Nov 1986.

[41] J. Eggers and H. A. Stone. Characteristic lengths at moving contact lines for a perfectly wetting fluid: the influence of speed on the dynamic contact angle. *J. Fluid Mech.*, 505:309, 2004.

[42] M. Ghosh and K. J. Stebe. Spreading and retraction as a function of drop size. *Advances in Colloid and Interface Science*, 161:61, 2010.

[43] A.-L. Biance, C. Clanet, and D. Quéré. First steps in the spreading of a liquid droplet. *Physical Review E*, 69:016301, 2004.

[44] S. Jung and I. M. Hutchings. The impact and spreading of a small liquid drop on a non-porous substrate over an extended timescale. *Soft Matter*, 8:2686, 2012.

[45] S. Mechkov, A. M. Cazabat, and G. Oshanin. Post-tanner stages of droplet spreading: the energy balance approach revisited. *Journal of Physics: Condensed Matter*, 21:464131, 2009.

[46] J. R. Barone. Evaluation of polymer rheology from drop spreading experiments. *Chemical Engineering Science*, 60:2579, 2005.

[47] S. I. Betelú and M. A. Fontelos. Capillarity driven spreading of circular drops of shear-thinning fluid. *Mathematical and Computer modelling*, 40:729, 2004.

[48] B. S. Dandapat and S. K. Singh. Spreading of a non-newtonian liquid drop over a horizontal plance. *Chemical Engineering Science*, 65:3427, 2010.

[49] A. Carré and F. Eustache. Spreading kinetics of shear-thinning fluids in wetting and dewetting modes. *Langmuir*, 16:2936, 2000.

[50] B. Davidovitch, E. Moro, and H. A. Stone. Spreading of viscous fluid drops on a solid substrate assisted by thermal fluctuations. *Phys. Rev. Lett.*, 95:244505, 2005.

[51] L. Bacri and G. Debregeas. Experimental study of the spreading of a viscous droplet on a nonviscous liquid. *Langmuir*, 1(7):6708, 1996.

[52] P.-G. de Gennes. Spreading of viscous droplets on a non viscous liquid. *Polymer*, 72:70, 1996.

[53] J. Fraaije and A. M. Cazabat. Dynamics of spreading on a liquid substrate. *Journal of Colloid and Interface Science*, 133:452, 1989.

[54] N. Alleborn and H. Raszillier. Spreading and sorption of a droplet on a porous substrate. *Chemical Engineering Science*, 59:2071, 2004.

[55] F. Pierce, D. Perahia, and G. S. Grest. Spreading of liquid droplets on permeable polymeric surfaces. *Europhysics Letters*, 86:64004, 2009.

[56] S. M. Kumar and A. P. Deshpande. Dynamics of drop spreading on fibrous porous media. *Colloids and Surfaces A*, 277:157, 2006.

[57] H. Haidara, B. Lebeau, C. Grzelakowski, L. Vonna, F. Biguenet, and L. Vidal. Competitive spreading versus imbibition of polymer liquid drops in nanoporous membranes: scaling behavior with viscosity. *Langmuir*, 24:4209, 2008.

[58] G. C. Berry and T. G. Fox. The viscosity of polymers and their concentrated solutions. *Adv. Polymer Sci.*, 5:261, 1968.

[59] G. Strobl. *The Physics of Polymers: Concepts for Understanding Their Structures and Behavior 2nd Edition.* Springer, 1996.

[60] M. L. Williams, R. F. Landel, and J. D. Ferry. The temperature dependnece of relaxation mechanisms in amorphous polymers and other glass-forming liquids. *J. Am. Chem. Soc.*, 77:3701, 1955.

[61] R. Howland and L. Benatar. *A Practical Guide to Scanning Probe Microscopy.* ThermoMicroscopes, 1998.

[62] R. M. A. Azzam and N. M. Bashara. *Ellipsometry And Polarized Light.* North-Holland, 1977.

[63] J. L. Carvalho, M. E. Somers, and K. Dalnoki-Veress. Ellipsometry as a probe of crystallization in binary blends of a sphere-forming diblock copolymer. *Journal of Polymer Science Part B: Polymer Physics*, 49:712, 2011.

[64] T. Salez, J. D. McGraw, S. L. Cormier, O. Bäumchen, K. Dalnoki-Veress, and E. Raphaël. *Numerical solutions of thin film equations for polymer flows, to be published elsewhere.*, 2012.

[65] J. D. McGraw, N. M. Jago, and K. Dalnoki-Veress. Capillary levelling as a probe of thin film polymer rheology. *Soft Matter*, 7:7832, 2011.

[66] O. Heavens. Optical properties of thin films. *Rep. Prog. Phys.*, 23, 1960.